

Pair cascades in the magnetospheres of strongly-magnetized neutron stars

Zach Medin^{1*} and Dong Lai^{2†}

¹*Department of Physics, McGill University, 3600 rue University, Montreal, QC H3A 2T8, Canada*

²*Department of Astronomy, Cornell University, Ithaca, NY 14853, USA*

ABSTRACT

We present numerical simulations of electron-positron pair cascades in the magnetospheres of magnetic neutron stars for a wide range of surface fields ($B_p = 10^{12}$ – 10^{15} G), rotation periods (0.1–10 s), and field geometries. This has been motivated by the discovery in recent years of a number of radio pulsars with inferred magnetic fields comparable to those of magnetars. Evolving the cascade generated by a primary electron or positron after it has been accelerated in the inner gap of the magnetosphere, we follow the spatial development of the cascade until the secondary photons and pairs leave the magnetosphere, and we obtain the pair multiplicity and the energy spectra of the cascade pairs and photons under various conditions. Going beyond previous works, which were restricted to weaker fields ($B \lesssim$ a few $\times 10^{12}$ G), we have incorporated in our simulations detailed treatments of physical processes that are potentially important (especially in the high field regime) but were either neglected or crudely treated before, including photon splitting with the correct selection rules for photon polarization modes, one-photon pair production into low Landau levels for the e^\pm , and resonant inverse Compton scattering from polar cap hot spots. We find that even for $B \gg B_Q = 4 \times 10^{13}$ G, photon splitting has a small effect on the multiplicity of the cascade since a majority of the photons in the cascade cannot split. One-photon decay into e^+e^- pairs at low-Landau levels, however, becomes the dominant pair production channel when $B \gtrsim 3 \times 10^{12}$ G; this tends to suppress synchrotron radiation so that the cascade can develop only at a larger distance from the stellar surface. Nevertheless, we find that the total number of pairs and their energy spectrum produced in the cascade depend mainly on the polar cap voltage $B_p P^{-2}$, and are weakly dependent on B_p (and P) alone. We discuss the implications of our results for the radio pulsar death line and for the hard X-ray emission from magnetized neutron stars.

Key words: radiation mechanisms: non-thermal – stars: magnetic fields – stars: neutron – pulsars: general.

1 INTRODUCTION

The pair cascade in the magnetosphere of a pulsar has long been considered an essential ingredient for the pulsar’s nonthermal emission, from radio to gamma rays (e.g., Sturrock 1971; Ruderman & Sutherland 1975; Melrose 2004; Thompson 2004). More recently it has been suggested that the pair cascade is also necessary for nonthermal emission from magnetars (e.g., Beloborodov & Thompson 2007; Thompson 2008a,b; see Woods & Thompson 2006 for a review of magnetars). The basic pair cascade involves several steps: (i) acceleration of primary particles by an electric field

parallel to the magnetic field; (ii) gamma ray emission by the accelerated particles moving along the magnetic field lines (either by curvature radiation or inverse Compton upscattering of surface photons); (iii) field-assisted photon decay into electron-positron pairs as the angle between the photon and the magnetic field line becomes sufficiently large, or pair production by two-photon annihilation in weak-field regimes; (iv) gamma ray emission by the newly-created particles as they lose their transverse energy through synchrotron emission; (v) further pair production and gamma ray emission via steps (iii) and (iv). The dense, relativistic (Lorentz factors $\gamma \gtrsim 100$) electron-positron plasma generated by this cascade is a required input in many models for the pulsar radio emission (e.g., Melrose 1995, 2004; Beskin 1999; Melikidze, Gil, & Pataraya 2000; Lyubarsky

* Email: zmedin@physics.mcgill.ca

† Email: dong@astro.cornell.edu

2002, 2008; Lyutikov 2007), while the high-energy photons emitted in pair cascade models can reproduce the observed pulse profiles and phase-resolved spectra of gamma-ray pulsars once the three-dimensional emission geometry is taken into account (see, e.g., Romani & Yadigaroglu 1995; Cheng, Ruderman, & Zhang 2000; Dyks & Rudak 2003; Harding et al. 2008; Bai & Spitkovsky 2009). We note in passing that the dense pair plasma generated by this cascade also plays an important role in models of pulsar wind nebulae (see Arons 2007 for a review).

The behavior of the pair cascade in the superstrong field regime (magnetic field strengths $B \gtrsim B_Q \equiv 4.414 \times 10^{13}$ G) and its effect on emission from pulsars and magnetars is somewhat puzzling. For example, of the dozen-or-so observed magnetars, only two show pulsed radio emission, and it is of a completely different nature than the emission from “standard” radio pulsars (e.g., the radio pulsations are transient and appear to be correlated with strong X-ray outbursts from the magnetars; see Camilo et al. 2007, 2008). In contrast, several radio pulsars with inferred surface field strengths similar to those of magnetars have been discovered (e.g., Kaspi & McLaughlin 2005; Vranevsevic, Manchester, & Melrose 2007). Why the standard mechanism for pulsed radio emission turns off for magnetars but not for these pulsars is unknown.

There have been only a few publications devoted to numerical simulations of the pair cascade in pulsar magnetospheres. For moderate-strength magnetic fields ($B \lesssim 5 \times 10^{12}$ G), significant progress has been made. Daugherty & Harding (1982) present simulations of the cascade initiated by a single electron injected from the neutron star surface, emitting photons through curvature radiation, for (polar) surface field strengths B_p up to 5×10^{12} G and rotation periods $P = 0.033$ –1 s. In a later paper (Daugherty & Harding 1996) they consider gamma ray emission from the entire open-field-line region of the magnetosphere, using a simplified acceleration model and for Vela-like pulsar parameters ($B_p = 3 \times 10^{12}$ G and $P = 0.089$ s). Sturmer, Dermer, & Michel (1995) present a similar simulation to that of Daugherty & Harding, but for cascades initiated by electrons upscattering photons through the inverse Compton process (again for Vela-like parameters). Hibschan & Arons (2001b) develop a semi-analytic model of the inner gap cascade, both for curvature radiation-initiated and inverse Compton scattering-initiated cascades, applicable for $B \lesssim 3 \times 10^{12}$ G (see also Zhang & Harding 2000). Cascades occurring in the outer magnetosphere have also been simulated, by Romani (1996) for Vela- and Crab-like ($B_p = 4 \times 10^{12}$ G and $P = 0.033$ s) parameters (see also Cheng, Ho, & Ruderman 1986a,b; Cheng, Ruderman, & Zhang 2000).

However, for superstrong magnetic fields ($B \gtrsim B_Q \equiv 4.414 \times 10^{13}$ G) only limited aspects of the full cascades have been studied. For example, Arendt & Eilek (2002) simulate the cascade for $B_p \leq 10^{13}$ G and $P = 0.033$ s (for both a pure dipole and a more complex field geometry), but with the simplification that all photons radiated by the primary particle are emitted from the surface. Baring & Harding (2001) (see also Harding, Baring, & Gonthier 1997) use this same simplification to study the effects of photon splitting on the cascade for field strengths up to $B = 2 \times 10^{14}$ G (however, they assumed that both photon modes can split, and thus

overestimated the effect of photon splitting; see Section 3.2). Baring & Harding (2007) model the process of resonant inverse Compton scattering of photons from the neutron star surface (with the blackbody temperature $T = 6 \times 10^6$ K) in the same field range, but only for single scattering events (see also Dermer 1990). The magnetosphere acceleration zone in the superstrong, twisted field regime of magnetars is investigated analytically by Beloborodov & Thompson (2007) for cascades occurring in the closed field line region of the magnetosphere and by Thompson (2008a,b) in the open field line region.

In this paper we present numerical simulations of the pair cascade from onset to completion. Motivated by the lack of full cascade results for the superstrong field regime, and in light of the unexplained differences between the observed emission properties of high-field radio pulsars and magnetars, we run our simulations in magnetospheres with field strengths up to 10^{15} G. We consider several important factors that affect high-field cascades, including photon splitting, pair creation in low Landau levels, photon polarization modes (\perp or \parallel to the magnetic field direction), and resonant inverse Compton scattering. We use our simulations to generate spectra of the high-energy photons and the electron-positron plasma produced by the cascade. Additionally, we use our simulations to comment on the conditions for when the radio emission mechanism no longer operates in the neutron star magnetosphere, the so-called “pulsar death line” (e.g., Ruderman & Sutherland 1975; Chen & Ruderman 1993; Hibschan & Arons 2001a; Harding & Muslimov 2002; Harding, Muslimov, & Zhang 2002; Medin & Lai 2007). While the results of our simulation are most applicable to cascades occurring in the open field line region of the magnetosphere (since the primary particles are injected into the magnetosphere along open field lines), some of our results are also relevant to cascades occurring in the closed field line region for magnetars, e.g., the products of a cascade initiated by a photon injected into a non-dipole magnetosphere.

A necessary component of any pair cascade simulation is a model of the magnetosphere acceleration zone, or “gap”, where the cascade originates. In real magnetospheres of pulsars and magnetars, the acceleration of primary particles is coupled to the rest of the cascade (e.g., charged particles produced in the cascade can screen out the acceleration potential). However, there is significant uncertainty about the precise nature of the acceleration gap. A number of models have been proposed for the location of the gap, from inner magnetosphere accelerators (both “vacuum” and “space-charge-limited flow” types; see, e.g., Ruderman & Sutherland 1975; Arons & Scharlemann 1979; Muslimov & Tsygan 1992; Hibschan & Arons 2001a; Medin & Lai 2007; Thompson 2008a,b), to outer magnetosphere accelerators (e.g., Cheng et al. 1986a,b; Romani 1996; Cheng et al. 2000; Takata et al. 2006), to hybrid inner-outer magnetosphere accelerators (“slot” gaps and extended outer gaps; e.g., Arons 1983; Muslimov & Harding 2003, 2004; Hirovani 2006). Non-steady (oscillatory) inner gaps have also been discussed recently (e.g., Sakai & Shibata 2003; Levinson et al. 2005; Beloborodov 2008; Luo & Melrose 2008). Numerical simulations of force-free global magnetospheres including magnetic-field twisting near the light cylinder have been performed (e.g., Contopoulos, Kazanas, & Fendt

1999; Gruzinov 2005; Spitkovsky 2006; Timokhin 2006; Komissarov 2006; Kalapotharakos & Contopoulos 2009), but they do not yet include any particle acceleration, or pair creation self-consistently. Therefore, in this paper we decouple particle acceleration from the rest of the cascade and focus on the cascade produced by a primary electron¹ injected into the magnetosphere with a given initial Lorentz factor γ_0 (cf. Daugherty & Harding 1982). We also consider the cascade produced by a single “primary” photon emitted by the primary electron, in the case where photon emission within the acceleration gap is important (i.e., for cascades where the dominant mechanism for high-energy photon production is inverse Compton scattering).

The outline of the paper is as follows. In Section 2 we summarize our method for estimating the initial parameters (e.g., γ_0) of the primary cascade particles, for use in our simulations. In Section 3 we describe the details of the numerical simulations, both for cascades with photon production dominated by curvature radiation and by resonant inverse Compton scattering (resonant ICS, or RICS). In Section 4 we present our results (e.g., photon and pair plasma spectra) for a wide range of parameters: surface magnetic fields $B = 10^{12}$ – 10^{15} G, rotation periods 0.1–10 s, surface temperatures $T = (0.3$ – $3) \times 10^6$ K, and pure dipole and more complex field geometries. In Section 5 we summarize our findings and discuss their implications for the radio emission and high-energy (hard X-ray and gamma-ray) emission from pulsars and magnetars. Some technical details (on our treatment of inverse Compton scattering, on our treatment of attenuation coefficients and e^+e^- energy levels for pair production, and on deriving semi-analytic fits to our numerical results) are given in the appendix.

2 ESTIMATING THE INITIAL PARAMETERS FOR THE PRIMARY PARTICLES

2.1 Primary electrons

In our cascade simulation (described in Section 3) we do not include an actual acceleration region, since we wish in this work to remain as model-independent as possible. Instead, we model the effect of this region on the cascade by giving the primary electron an initial energy $\gamma_0 m_e c^2$ equivalent to the energy it would reach upon traversing the entire gap, and injecting it into the magnetosphere at the neutron star surface (cf. Daugherty & Harding 1982). Obviously, this approximation excludes a proper treatment of the slot gap and outer gap acceleration models. However, in most parts of the polar cap region (i.e., except for the boundary region adjacent to the open field lines), the main voltage drop occurs near the stellar surface, regardless of the nature of the “gap” (vacuum gap or space charge limited flow). Such inner gap models and other global models with near-surface acceleration are allowed in our analysis.

For a dipole magnetic field geometry, most active pulsars with inner gap accelerators have gap voltage drops in

the range $\Phi \sim (1$ – $2) \times 10^{13}$ V, regardless of the acceleration model (e.g., Hibschan & Arons 2001a; Medin & Lai 2007, hereafter ML07). For the surface field strengths we are considering, $B \geq 10^{12}$ G, the primary electrons are not radiation-reaction limited within these gaps (ML07; cf. the millisecond pulsar models of Harding, Usov, & Muslimov 2005), so we can set $\gamma_0 = e\Phi/m_e c^2$. We therefore restrict γ_0 to the range $(2$ – $4) \times 10^7$ for dipole fields. Note that these large voltage drops do not occur in pulsars where the gap electric field is fully screened due to inverse Compton scattering by the primary electron. We discuss this case in Section 2.2.

The voltage drop across the gap can be no larger than the voltage drop across the entire polar cap of the neutron star (e.g., Ruderman & Sutherland 1975):

$$\Phi_{\text{cap}} \simeq \frac{\Omega B_p R^3 \Omega}{2c} = 7 \times 10^{12} B_{p,12} P_0^{-2} \text{ V}, \quad (1)$$

where R is the radius of the star (assumed in this paper to be 10 km), P_0 is the spin period in units of 1 s, and $B_p = 10^{12} B_{p,12}$ G is the polar surface magnetic field strength. If the voltage drop, Φ , required to initiate pair cascades is not available, i.e., $\Phi > \Phi_{\text{cap}}$, the magnetosphere should not produce pulsed radio emission; the locus of points where $\Phi = \Phi_{\text{cap}}$ defines the pulsar death line.² A typical death line for an inner gap model, plotted in P - \dot{P} space, is shown on the left panel of Fig. 1. The line was made using three assumptions: (i) The magnetosphere field geometry is dipolar. (ii) The pair cascade occurs primarily above the gap, (through curvature radiation) once the primary electron has reached a large Lorentz factor $\gamma_0 \sim 10^7$. (iii) The spindown power of the pulsar, given by

$$\dot{E} = -I\Omega\dot{\Omega} = \frac{4\pi^2 I \dot{P}}{P^3}, \quad (2)$$

is approximately equal to the spindown power of a magnetic dipole with its magnetic field and rotational axes orthogonal to each other:

$$\dot{E} \simeq \frac{B_p^2 \Omega^4 R^6}{6c^3} = \frac{2\Phi_{\text{cap}}^2 c}{3}. \quad (3)$$

The polar magnetic field strength inferred from this frequently-used approximation is

$$B_{p,12} \simeq 2.0 \sqrt{P_0 \dot{P}_{-15}}, \quad (4)$$

where \dot{P}_{-15} is the period derivative in units of 10^{-15} s/s and $I = 10^{45}$ g-cm² is assumed.

A well-known problem with the death line made using these assumptions is that it cuts right through the middle of the main group of pulsars (Ruderman & Sutherland 1975; Hibschan & Arons 2001a; Harding & Muslimov 2002; Medin & Lai 2007); i.e., the model incorrectly predicts that there will be no radio emission from many neutron stars that are observed to be active pulsars.

Several authors have proposed models of the neutron star magnetosphere that shift the theoretical death line closer to the observed death line by altering one

¹ Although the primary particle could also be a positron (or even an ion), we assume here for simplicity that the pulsar is oriented such that electrons are accelerated away from the star.

² This applies to the vacuum gap model. In the space-charge-limited-flow model the condition is $\Phi = \kappa_g \Phi_{\text{cap}}$, with $\kappa_g \simeq 0.15$ (e.g., Hibschan & Arons 2001a).

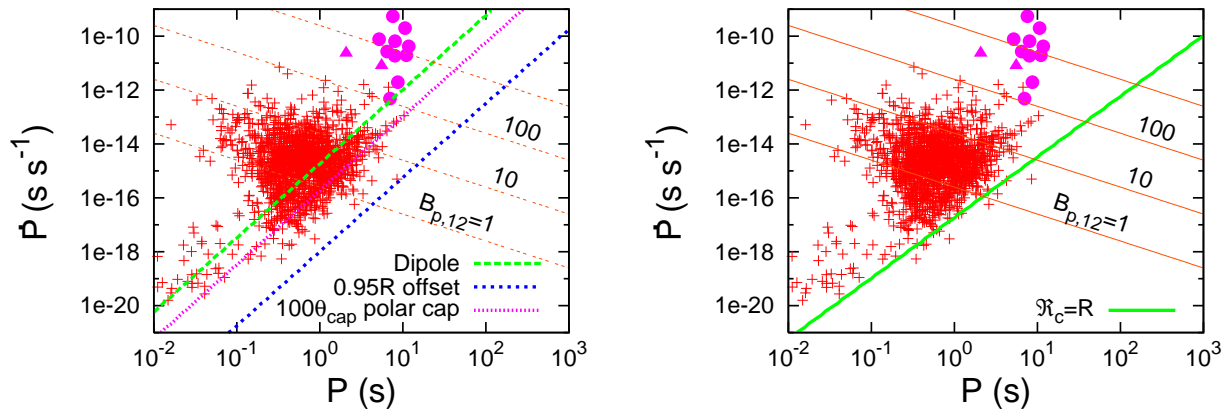


Figure 1. Pulsar death lines. Death lines are shown for pulsars with dipole magnetic fields, dipole fields offset from the center of the star by $\Delta r = 0.95R$, and magnetic fields with extended polar caps 100 times larger than the dipole value $\theta_{\text{cap}} = \sqrt{\Omega R/c}$ (left panel); and for pulsars with magnetic field curvatures $\mathcal{R}_c = R$ at the surface (right panel). Note that these death lines do not apply for the millisecond pulsar population in the lower left corner of the diagram, as their short periods and low magnetic field strengths cause the primary electron to be radiation reaction limited. In each panel, rotation-powered pulsars (ATNF catalog, <http://www.atnf.csiro.au/research/pulsar/psrcat>) are labeled by crosses, while magnetars (McGill catalog, <http://www.physics.mcgill.ca/~pulsar/magnetar/main.html>) are labeled by solid circles and the two radio magnetars are labeled by solid triangles.

or more of the assumptions made above. In some models the magnetosphere geometry is not a centered dipole, but instead is an offset dipole (Arons 1998), or a twisted dipole (e.g., Thompson, Lyutikov, & Kulkarni 2002), or contains quadrupole or higher multipole components (e.g., Pavan et al. 2009). Numerical simulations suggest that due to twisting of the field lines near the light cylinder the polar cap is slightly larger than in the pure dipole case (e.g., Contopoulos et al. 1999; Spitkovsky 2006); the polar cap could be significantly larger if, as the pulsar spins down, field line reconnection (conversion of open field lines into closed field lines) is too slow to keep pace with the expanding light cylinder (Contopoulos 2005). All of these models increase the size of the theoretically allowed P - \dot{P} space for pulsars by decreasing the radius of curvature of the magnetic field lines \mathcal{R}_c in the region where the pair cascade occurs, i.e., above the polar cap. Since pair creation is more efficient along tightly-curved field lines, a smaller radius of curvature allows the cascade to occur at a lower γ_0 . However, the magnetosphere must be highly non-dipolar near the polar cap in order for the models to include all pulsars on the active side of the death line. For example, the offset dipole model can fully match observation only if the dipole is offset by $0.95R$ or more, while an expanded polar cap (due to a twisted field or delayed field reconnection) must be hundreds of times larger than the pure dipole cap; see Fig. 1. It is unclear whether such a strongly non-dipolar field is stable (cf. Beloborodov & Thompson 2007, where a field twist $\Delta\phi \gtrsim 1$ radian is unstable even in magnetars). In addition, observations of pulsar radio emission suggest that this emission is coming from a purely dipole region of the magnetosphere (e.g., Rankin & Wright 2003), so any non-dipole structure at the surface must give way to a dipole configuration at the altitude where radio pulses are generated (typically about 1% of the light cylinder radius; e.g., Gangadhara & Gupta 2001; Dyks, Rudak, & Harding 2004). In our simulation, we model the effects of a non-dipole magnetosphere by giving the magnetic field a large curvature

($\mathcal{R}_c = R$; cf. Ruderman & Sutherland 1975) at the surface and a dipole curvature at higher altitudes ($r > 2R$); the implementation of this non-dipole model into our simulation is discussed in more detail in Section 3. The death line in this approximation is shown on the right panel of Fig. 1. Because of the increased efficiency of the cascades in these highly-curved magnetic fields, the Lorentz factor of the primary electron upon emerging from the gap is a factor of ~ 10 lower than in the dipole case, in the range $\gamma_0 \simeq (2-4) \times 10^6$ (Hibschman & Arons 2001a; Medin & Lai 2007).

In some models the pair cascade occurs primarily within the gap, due to efficient inverse Compton scattering by the primary electron, rather than above the gap. These cascades occur at much lower energies of the primary electron ($\gamma \sim 10^3-10^4$), such that all observed pulsars can provide the voltage necessary to initiate this type of cascade. However, ICS cascades are generally very weak, producing $\lesssim 10$ electron-positron pairs per primary electron, while most radio emission models assume a secondary particle density 100-1000 times that of the primary electron beam (e.g., for the development of a two-stream instability; see Usov 2002). The inclusion of this type of cascade into our simulations is discussed below, in Section 2.2.

In some models the spindown power of the neutron star differs from that of an orthogonal magnetic dipole, Eq. (3). For example, Contopoulos & Spitkovsky (2006) show that for nearly-aligned pulsars (with the angle between the magnetic field and rotation axes $\alpha \lesssim 30^\circ$), the spindown power can be approximated by

$$\dot{E} \simeq \frac{2\Phi_{\text{cap}}^2 c}{3} \left(1 - \frac{\Phi}{\Phi_{\text{cap}}}\right). \quad (5)$$

This equation is nearly the same as Eq. (3) for young pulsars, where $\Phi \ll \Phi_{\text{cap}}$. However, for pulsars near death, with $\Phi \lesssim \Phi_{\text{cap}}$, the spindown power is much lower for a given polar cap voltage. Conversely, for a given P and \dot{P} [which determines the observed spindown power, Eq. (2)] the polar cap voltage is much larger than would be assumed by us-

ing Eq. (3). Depending on alignment and how close the gap potential drop Φ is to Φ_{cap} , many pulsars which were predicted to be dead may actually have a potential drop large enough to generate pair cascades ($\Phi \simeq 10^7$ V). According to Contopoulos & Spitkovsky, the standard death line shown in Fig. 1 is consistent with the observed $P-\dot{P}$ values for all pulsars if the magnetic inclination angles α of nearly-dead pulsars are weighted towards $\alpha = 0$. If this is the case, we can use $\gamma_0 \simeq (2-4) \times 10^7$ for all pulsars and do not need to invoke a strongly-curved magnetic field geometry ($\mathcal{R}_c \simeq R$) or efficient inverse Compton scattering by the primary electron in order to reproduce the observed pulsar death line.

2.2 Primary photons

As the primary electron traverses the acceleration region it can pass through two distinct regimes (see, e.g., Hibschan & Arons 2001a). First, for Lorentz factors $\gamma \sim 10^2-10^4$, the electron efficiently upscatters photons through the inverse Compton process. Second, for Lorentz factors $\gamma \gtrsim 10^6$, the electron efficiently emits curvature radiation. The above treatment of the acceleration zone (Section 2.1) is best suited for pulsars where the electrons reach the second regime. In that case we can safely ignore the contributions to the cascade made by photons emitted before the primary electron reaches full energy (γ_0), since the number and energy of photons emitted through curvature radiation increase strongly with γ (i.e., $\dot{N}_{\text{CR}} \propto \gamma$, $E_{\text{CR}} \propto \gamma^3$). The approximation is poor, however, if inverse Compton scattering and subsequent pair production within the gap is efficient enough to screen the accelerating potential before the electrons can reach the second regime. In that case the photons produced in the gap are critical to the cascade, while the photons produced above the gap have a negligible effect on the cascade (the upscattered photons must travel a finite distance before pair production in order to screen the gap; in that distance the primary electron is accelerated to above resonance and exits the gap with a Lorentz factor between the first and second regimes of efficient photon production).

Because ICS is strongly peaked at resonance, primary electrons traveling through this second type of gap will emit a large number of photons at a characteristic “resonance” energy and very few at other energies. The effect of this type of gap on the cascade is better modeled by N_0 photons of energy ϵ_0 emitted from the surface (cf. Arendt & Eilek 2002), rather than one electron of energy $\gamma_0 m_e c^2$. We therefore run a second version of the simulation, this time tracking the cascade initiated by a “primary” photon. The quantitative results of this simulation can be multiplied by N_0 to obtain the full cascade results (e.g., the number of electron-positron pairs produced per primary electron).

For a primary electron resonantly upscattering primary photons, we estimate the value of ϵ_0 as follows. When the primary electron reaches a Lorentz factor γ , it upscatters photons to a mean energy (e.g., Beloborodov & Thompson 2007)

$$\epsilon = \gamma \left(1 - \frac{1}{\sqrt{1 + 2\beta_Q}} \right) m_e c^2, \quad (6)$$

where $\beta_Q = B/B_Q$ is the ratio of the magnetic field strength to the critical quantum field strength, $B_Q = 4.414 \times 10^{13}$ G.

The primary electron is most efficient at scattering photons when

$$\gamma = \gamma_{\text{crit}} \simeq \epsilon_c / kT, \quad (7)$$

where T is the surface temperature of the star and $\epsilon_c = \hbar e B / m_e c$ is the electron cyclotron energy.³ Therefore, for photons scattered from near the surface, where $B = B_p$, the typical energy of a scattered photon is

$$\epsilon_{\text{RICS}} \simeq 70 B_{p,12} T_6^{-1} f(\beta_Q) \text{ MeV}, \quad (8)$$

where T_6 is the surface temperature in units of 10^6 K and $f(\beta_Q) = 1 - 1/\sqrt{1 + 2\beta_Q}$ is evaluated at the surface. Setting $\epsilon_0 = \epsilon_{\text{RICS}}$ and assuming a T_6 range of 0.3–3, we obtain ϵ_0 in the range 1–10 MeV at $B_{p,12} = 1$ up to $(0.4-4) \times 10^5$ MeV at $B_{p,12} = 1000$.

The number of resonant ICS photons scattered by the primary electron is more difficult to estimate, since it depends on the acceleration model. Inner gaps with space-charge-limited flows have (e.g., Hibschan & Arons 2001a; Medin 2008)

$$N_0 \simeq 10 B_{p,12}^{-1} P_0^{3/4} T_6^{5/2}. \quad (9)$$

Inner vacuum gaps, with accelerating electric fields on the order of 6 times larger, have N_0 values at least 20–100 times smaller (the primary electron is more rapidly accelerated out of resonance; see, e.g., ML07).

Note that we can also use this second cascade simulation as a diagnostic tool for the main simulation. For example, we can study the partial cascade initiated by a single curvature radiation photon emitted at some altitude in the magnetosphere to understand how the strength of the local magnetic field affects the cascade. The characteristic energy of curvature photons is

$$\epsilon_{\text{CR}} = \frac{3\gamma^3 \hbar c}{2\mathcal{R}_c}. \quad (10)$$

For dipole fields the typical curvature photon has an energy $\epsilon_{\text{CR}} \lesssim 10^3-10^4$ MeV (for $\gamma \leq \gamma_0 \sim 10^{7.5}$), while for fields with $\mathcal{R}_c = R$ we have $\epsilon_{\text{CR}} \lesssim 10^2-10^3$ MeV (for $\gamma \leq \gamma_0 \sim 10^{6.5}$).

3 NUMERICAL SIMULATION OF PAIR CASCADES: PHYSICS INGREDIENTS AND METHODS

The general picture of the pair cascade as modeled by our numerical simulation is sketched in Fig. 2. At the start of the simulation, an electron with initial Lorentz factor $\gamma_0 \sim 10^{6.5}-10^{7.5}$ (Section 2.1) travels outward from the stellar surface along the last open field line. As it travels it emits high-energy photons through curvature radiation or inverse Compton upscattering. The simulation tracks these photons

³ Note that the actual resonance condition is $\epsilon_i \gamma (1 - \beta \cos \psi) = \epsilon_c$, where $\epsilon_i \sim kT$ is the initial (before scattering) photon energy, $\beta = \sqrt{1 - 1/\gamma^2}$ is the ratio of the electron speed to the speed of light and ψ is the incident angle of the photon with respect to the electron’s trajectory. However, because the scattering rate depends inversely on γ (see Appendix A), photons with $\cos \psi \ll 1$ are far more likely to scatter off the electron than photons with $\cos \psi \lesssim 1$.

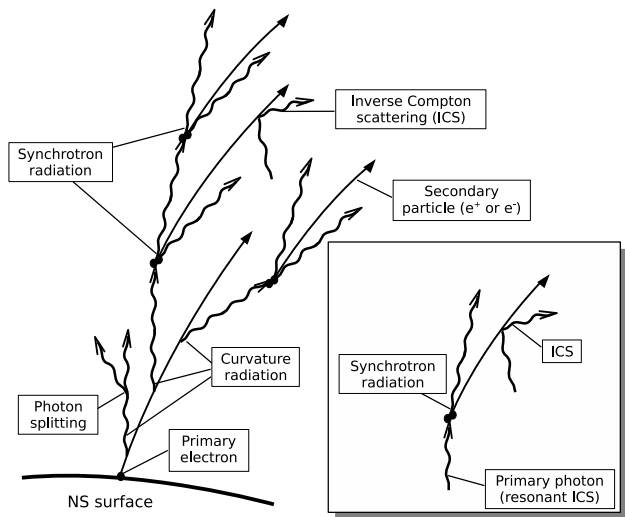


Figure 2. A schematic diagram showing the magnetosphere pair cascade, from initiation by a high-energy electron to completion. Photon splitting is also shown. The inset shows the beginning of a cascade initiated by a photon upscattered through the inverse Compton process.

as they propagate from the point of emission through the magnetosphere, until they decay into electron-positron pairs through magnetic pair production or escape to infinity. In the superstrong field regime, the photon (if it has the correct polarization; see Section 3.2) also has a finite probability of splitting into two photons before pair production, in which case we follow the two child photons in a similar way. The electrons and positrons created by these photons are tracked as they radiate away their transverse momenta through synchrotron radiation and then gradually lose their forward momenta through inverse Compton scattering. Subsequent generations of photons and electrons/positrons are also tracked, in a recursive manner, and the total numbers and energies of photons and electrons + positrons that escape the magnetosphere are recorded. We track each particle until it is destroyed or reaches a height comparable to the light cylinder radius. Tracking particles out to the light cylinder is most important for the primary electron, since although in general there is no discernible pair production above the radius $r \sim 10R$, curvature radiation continues up to very high altitudes (albeit very weakly, with photon energies $\epsilon \lesssim 10$ MeV near the light cylinder).

In the second version of our cascade simulation, a photon with energy $\epsilon_0 \sim 10^3\text{--}10^5$ MeV (see Section 2.2) travels outward from the last open field line at the stellar surface, in the direction tangent to the magnetic field at that point. While in theory the photon should be emitted at an angle to the field line of $\Delta\Theta_{\text{ph}} \lesssim 1/\gamma_e$, where γ_e is the final Lorentz factor of the electron after emitting the photon, in practice this does not matter, as there is no change in the final products of the cascade whether we use $\Delta\Theta_{\text{ph}} = 1/\gamma_e$ or $\Delta\Theta_{\text{ph}} = 0$. (This is true even for photons upscattered by resonant ICS at $B \gtrsim B_Q$; see Section 3.3.2). The primary photon and subsequent generations of electrons/positrons and photons are tracked in the same way as in the main cascade simulation. The cascade as modeled by the second simulation is sketched in the inset of Fig. 2.

The input parameters for our simulation are the initial energy of the electron ($\gamma_0 m_e c^2$) or photon (ϵ_0), its initial position (in most cases, the intersection of the last open field line with the stellar surface), the general pulsar parameters (surface magnetic field strength $B_p = 10^{12}\text{--}10^{15}$ G, rotation period $P = 0.33\text{--}5$ s, and surface temperature $T = 10^6$ K or 5×10^6 K), and the geometry of the magnetic field. In each run of the simulation, the magnetic field structure is given by one of two topologies: (i) a pure dipole field geometry; or (ii) a more complex field geometry near the stellar surface which gradually reverts to dipole at higher altitudes (a non-dipole, or “multipole” field geometry). Modeling the dipole field geometry is straightforward (see, e.g., von Hoensbroech, Lesch, & Kunzl 1998), but there is no obviously correct way to model the geometry for the multipole field case (see Section 2.1). Two features of a multipole field geometry have a strong effect on the pair cascade dynamics and must be incorporated into our model: First, the radius of curvature \mathcal{R}_c is much smaller than dipole (we choose $\mathcal{R}_c = R$, the stellar radius) near the surface of the star. This leads to a much larger number and peak energy of photons emitted through curvature radiation than in the dipole field case. Second, as a photon propagates through the magnetosphere the angle between the photon and the field, which scales like $\Delta\Theta_{\text{ph}} \sim s_{\text{ph}}/\mathcal{R}_c$, where s_{ph} is the distance traveled by the photon from the point of emission, grows much faster than dipole. This leads to a much more rapid decay of photons into pairs than in the dipole case. The integration of these two features into our model is discussed in the relevant subsections below (Section 3.1 and Section 3.2, respectively). Note that Arendt & Eilek (2002) consider the first aspect of a multipole field geometry in their model (that $\mathcal{R}_c = R$) but ignore the second. In all of the simulation runs we assume that the local magnetic field strength varies as in the dipole case,

$$B(r, \theta, \phi) = B_p \left(\frac{R}{r} \right)^3 \frac{\sqrt{3 \cos^2 \theta + 1}}{2}, \quad (11)$$

where (r, θ, ϕ) are the spherical coordinates (with the magnetic north pole at $r = R$ and $\theta = 0$). Our approximation therefore ignores any amplification of the field strength near the surface caused by the complex topology.

For simplicity we consider a “two-dimensional” cascade model in which all photons are emitted and travel in the plane defined by the local magnetic field line. Both the photons and the electrons/positrons are tracked in the “corotating” frame (the frame rotating with the star), and any bending of the photon path due to rotation is ignored – this is expected to be valid since the cascade takes place far inside the light cylinder. Thus we shall also call this corotating frame the “lab” frame for the remainder of the paper. With this approximation the particle positions and trajectories are defined only in terms of r and θ in our simulation. We justify this approximation below (Sections 3.1 and 3.2). As an additional simplification we ignore any effects of general relativity on the photon/particle trajectory.

The cascade simulation can naturally be divided into three parts: (i) the propagation and photon emission of the primary electron; (ii) photon propagation, pair production, and splitting; and (iii) the propagation and photon emission

of the secondary⁴ electrons and positrons. Each of these aspects of the simulation is described in a separate subsection below. At the end of this section, cascades initiated by primary photons are discussed.

3.1 Propagation and photon emission of the primary electron

In our cascade simulation, the primary electron starts at the position $(r_0, \theta_0) = (R, \theta_0)$ (i.e., at some angle θ_0 from the magnetic pole on the neutron star surface) with the initial energy $\gamma_0 m_e c^2$, and moves outward along the local magnetic field line. The initial position of the primary electron is chosen so that it moves along the last open field line, whose location at the surface is given by the polar cap angle: $\theta_0 = \theta_{\text{cap}} \equiv \sqrt{R/r_{\text{LC}}}$, where $r_{\text{LC}} = c/\Omega$ is the light cylinder radius.⁵

The primary electron moves outward along the field line in a stepwise fashion. The lengths of the steps $\Delta s(r)$ are chosen so that a uniform amount of energy $\Delta\gamma$ (we choose $\sim 0.001\gamma_0$) is lost by the electron in each step ($\gamma \rightarrow \gamma - \Delta\gamma$):

$$\Delta s(r) \simeq -\frac{\Delta\gamma}{d\gamma/ds}. \quad (12)$$

For an electron emitting curvature radiation,

$$\frac{d\gamma}{ds} = -\frac{2}{3}\gamma^4 \frac{\alpha_f^2 a_0}{\mathcal{R}_c^2}, \quad (13)$$

where $\alpha_f = e^2/(\hbar c)$ is the fine structure constant and a_0 is the Bohr radius. For a dipole field the radius of curvature is given by

$$\mathcal{R}_c = \frac{r}{\sin\theta} \frac{(1 + 3\cos^2\theta)^{3/2}}{3 + 3\cos^2\theta}, \quad (14)$$

while for a near-surface multipole field we use $\mathcal{R}_c = R$. As discussed in Section 2.1, we do not consider photon emission due to inverse Compton scattering here, since this process is very inefficient once the primary electron has reached the energy $\gamma_0 m_e c^2$. We do, however, consider in our simulation the photon emission due to ICS by the secondary electrons and positrons (see Section 3.3) which typically have $\gamma \ll \gamma_0$. Note that we also indirectly include ICS in our second cascade simulation (described in Section 3.4), which models photon-initiated cascades, by choosing photon energies ϵ_0 that are typical of ICS photons.

As the electron moves a distance Δs along the field it emits photons with energies divided into discrete bins (our simulation uses ~ 50 bins). The energy in each bin, ϵ , is a constant multiple of the characteristic energy of curvature

photons $\epsilon_{\text{CR}} = 3\gamma^3 \hbar c / (2\mathcal{R}_c)$, with $\epsilon/\epsilon_{\text{CR}}$ in the range 10^{-4} – 10 . The number of photons in a given energy bin emitted in one step is given by the classical spectrum of curvature radiation (e.g., Jackson 1998),

$$\Delta N_\epsilon \simeq \Delta\epsilon \frac{dN}{d\epsilon} \simeq \frac{\sqrt{3}}{2\pi} \frac{\alpha_f \Delta s}{\mathcal{R}_c} \frac{\gamma \Delta\epsilon}{\epsilon} F\left(\frac{\epsilon}{\epsilon_{\text{CR}}}\right), \quad (15)$$

where $\Delta\epsilon$ is the spacing between energy bins and the values of \mathcal{R}_c and γ used are averages over the interval Δs . Here, $F(x) = x \int_x^\infty K_{5/3}(t) dt$ and $K_{5/3}(x)$ is the $n = 5/3$ Bessel function of the second kind. Note that $F(x) \propto x^{1/3}$ for $x \ll 1$, and $F(x) \propto \sqrt{x} e^{-x}$ for $x \gg 1$ (e.g., Erber 1966).

The photons are emitted in the direction nearly tangent to the field line at the current location of the electron (r, θ) . For a dipole field geometry the angle between the local magnetic field and the magnetic dipole axis is given by

$$\chi(\theta) = \theta + \arctan\left(\frac{\tan\theta}{2}\right); \quad (16)$$

see Fig. 3. There is an additional contribution to the emission angle of $\sim 1/\gamma$, due to relativistic beaming. In reality this beaming angle is in a random direction; however, for our two-dimensional approximation it can only be in the plane of the magnetic field. The photon emission angle is given by the (projected) sum of these two angles:

$$\Theta_{\text{ph}} = \chi + \frac{1}{\gamma} \cos\Pi, \quad (17)$$

where Π is a random angle between 0 and 2π . Note that ignoring the three-dimensional aspect of the photon emission introduces an error in the emission angle of order $1/\gamma$. This affects the location at which the photon decays (into pairs) in our simulation, since photon decay depends strongly on the intersection angle between the photon and the magnetic field (see Section 3.2 below). However, as the photon propagates through the magnetosphere these errors (which are on the order of $1/\gamma \sim 10^{-7}$ for curvature photons and 10^{-3} for resonant ICS photons) quickly become negligible in comparison to the photon-magnetic field intersection angle, which grows like $s_{\text{ph}}/\mathcal{R}_c$ (and so reaches the angle $1/\gamma$ by $s_{\text{ph}} \sim 10^{-5}R$ for curvature radiation and $\sim 0.1R$ for RICS).

We also use Eq. (17) for simulation runs with a multipole field geometry. This is obviously a simplification, but we have found that in practice the photon propagation direction has little effect on the overall cascade product (as long as it points generally outward). Far more important for the cascade is how the angle between the photon and the magnetic field changes as the photon travels. As is discussed in Section 3.2, we artificially force this angle to change more rapidly with distance than in the dipole case, to account for the effect of the stronger field line curvature.

The total energy lost over each step is

$$\sum_\epsilon \epsilon \Delta N_\epsilon \simeq \Delta\gamma m_e c^2. \quad (18)$$

Only one photon is tracked for each energy bin ϵ at each step Δs , so the photon is given a weighting factor ΔN_ϵ . In addition to its initial position (the position of the electron at the point of emission r, θ) and propagation direction (Θ_{ph}), the photon has a polarization direction. For curvature radiation the polarization fraction is between 50% and 100% polarized parallel to the magnetic field curvature, depending on photon frequency (Jackson 1998; see also Rybicki & Lightman

⁴ In this paper we use the term “secondary” to refer to any cascade particle except the primary electron, positron, or photon that initiates the cascade. The fourth generation of electrons and positrons, e.g., are all “secondary” particles.

⁵ Since the last open field line is also the most-tightly curved, this choice for the primary electron’s location gives us the largest possible cascade in our simplified model. However, in a real magnetosphere there is no cascade at all along the last open field line and weak cascades for field lines very near the last ($\theta \lesssim \theta_{\text{cap}}$), since the potential drop is zero on the boundary of the open field region. The strongest cascades occurs on field lines neither at the edge of the open field region nor at the center (where $\mathcal{R}_c \rightarrow \infty$).

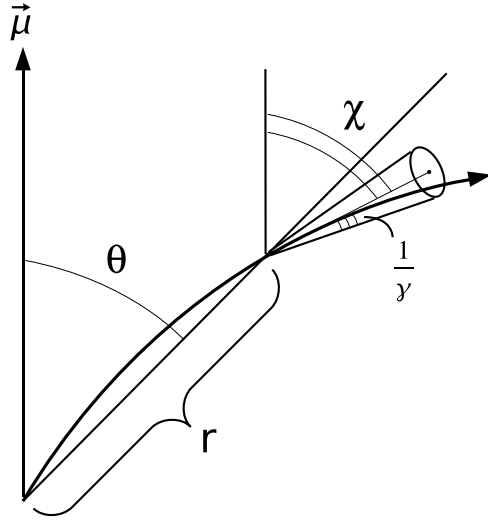


Figure 3. A schematic diagram illustrating the photon emission angle. The direction of the magnetic dipole axis is given by $\vec{\mu}$. The electron (positron) follows the curved field line to the point (r, θ) , then emits a photon in a cone of width $1/\gamma$, inclined with respect to the magnetic axis by an angle χ .

1979). We therefore randomly assign the photon a polarization in the ratio of one \perp (perpendicular to the field) to every seven \parallel (parallel to the field) photons, corresponding to 75% averaged parallel polarization.

3.2 Photon propagation, pair production, and splitting

In our simulation, the photon is emitted/scattered from the point $(r_{0,\text{ph}}, \theta_{0,\text{ph}})$ with energy ϵ , polarization \parallel or \perp , and weighting factor ΔN_ϵ (to represent multiple photons; Section 3.1). It has an optical depth to pair production, τ , and to photon splitting, τ_{sp} , both of which are set to zero at the moment of the photon's creation. The photon propagates in a straight line from the point of emission, at an angle Θ_{ph} with respect to the magnetic dipole axis. Note that in the corotating frame (which is the frame we are working in for most of our simulation; but see Section 3.3) the path of the photon is in reality curved, with the angular deviation from a straight line growing approximately as $s_{\text{ph}}\Omega/c = s_{\text{ph}}/r_{\text{LC}}$ (cf. Harding, Tademaru, & Esposito 1978). Like the beaming angle (Section 3.1), this curved path modifies the growth of the photon-magnetic field intersection angle and the location of photon decay in our simulation. However, the total intersection angle grows much faster with photon distance s_{ph} than the deviation does ($\sim s_{\text{ph}}/\mathcal{R}_c$ versus $s_{\text{ph}}/r_{\text{LC}}$, or a factor of $r_{\text{LC}}/\mathcal{R}_c \simeq 100P_0^{1/2}$ larger for dipole fields), so we can safely ignore this deviation.

In each step the photon travels a short distance through the magnetosphere, $\Delta s_{\text{ph}} < 0.05r_{\text{ph}}$, where $(r_{\text{ph}}, \theta_{\text{ph}})$ refers to the current position of the photon; our method for choosing the value of Δs_{ph} for a given photon is discussed at

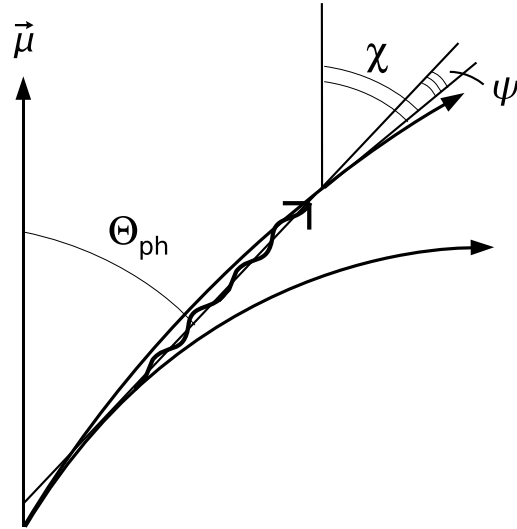


Figure 4. A schematic diagram for deriving the angle between the photon and the magnetic field, ψ . The direction of the magnetic dipole axis is given by $\vec{\mu}$. The photon propagates through the magnetosphere with angle Θ_{ph} with respect to the magnetic axis [see Eq. (17)]. The local magnetic field makes an angle χ with respect to the magnetic axis [Eq. (16)].

the end of this section. At the new position the change in the optical depth for pair production, $\Delta\tau$, and for photon splitting, $\Delta\tau_{\text{sp}}$, are calculated:

$$\Delta\tau \simeq \Delta s_{\text{ph}} R_{\parallel,\perp}, \quad (19)$$

$$\Delta\tau_{\text{sp}} \simeq \Delta s_{\text{ph}} R_{\parallel,\perp}^{\text{sp}}, \quad (20)$$

where $R_{\parallel,\perp} = R'_{\parallel,\perp} \sin\psi$ is the attenuation coefficient for the \parallel or \perp polarized photons, ψ is the angle of intersection between the photon and the local magnetic field, and R' is the attenuation coefficient in the “perpendicular” frame (i.e., the frame where the photon propagates perpendicular to the local magnetic field). For a dipole field geometry the intersection angle is given by

$$\psi = \chi(\theta_{\text{ph}}) - \Theta_{\text{ph}}, \quad (21)$$

where Θ_{ph} is given by Eq. (17) and $\chi(\theta_{\text{ph}})$ is the angle between the magnetic axis and the magnetic field at the current location of the photon [Eq. (16)]; see Fig. 4 for a sketch. For the near-surface multipole field geometry we set

$$\tan\psi = \frac{s_{\text{ph}}}{\mathcal{R}_c} = \frac{s_{\text{ph}}}{R}. \quad (22)$$

This approximation has the advantage of accounting for the effect of a strong field curvature on the photon propagation without requiring knowledge of the actual field topology.

The total attenuation coefficient (in the perpendicular frame) for pair production is given by (suppressing the subscripts \parallel, \perp) $R' = \sum_{jk} R'_{jk}$, where R'_{jk} is the attenuation coefficient for the channel in which the photon produces an electron in Landau level j and a positron in Landau level k ,

and the sum is taken over all possible states for the electron-positron pair. Since pair production is symmetric with respect to the electron and the positron, $R'_{jk} = R'_{kj}$; for simplicity we hereafter use R'_{jk} to represent the combined probability of creating the pair in either the state (jk) or (kj) (i.e., $R'_{jk}^{\text{new}} = R'_{jk}^{\text{old}} + R'_{kj}^{\text{old}}$). For a given channel (jk) , the threshold condition for pair production is

$$\epsilon' > E_j + E_K, \quad (23)$$

where $\epsilon' = \epsilon \sin \psi$ is the photon energy in the perpendicular frame and $E_n = m_e c^2 \sqrt{1 + 2\beta_Q n}$ is the minimum energy of an electron/positron in Landau level n (the energy of an electron/positron with the momentum along the magnetic field $p_{\parallel} = 0$). In dimensionless form, the condition [Eq. (23)] can be written as

$$x = \frac{\epsilon'}{2m_e c^2} = \frac{\epsilon}{2m_e c^2} \sin \psi > x_{jk} \equiv \frac{1}{2} \left[\sqrt{1 + 2\beta_Q j} + \sqrt{1 + 2\beta_Q k} \right]. \quad (24)$$

Note that x_{jk} satisfies

$$x_{00} < x_{01} < x_{02} < \begin{cases} x_{11} < x_{03} < \dots, & \beta_Q < 4; \\ x_{03} < x_{11} < \dots, & \beta_Q > 4. \end{cases} \quad (25)$$

The first three attenuation coefficients (corresponding to the three lowest threshold levels x_{00}, x_{01}, x_{02}) for both \parallel and \perp polarizations are given in Appendix B, Eqs. (B6)-(B10); see also Daugherty & Harding (1983). Note that $R'_{\perp,00} = 0$, and thus the first non-zero attenuation coefficient for \perp polarized photons is actually $R'_{\perp,01}$, not $R'_{\perp,00}$.

In our simulation a photon is typically created with x below the first threshold (x_{00} or x_{01} , depending on the photon polarization). As long as x remains below the first threshold, $R' = 0$ and the optical depth to pair production remains zero. As the photon propagates into the magnetosphere and crosses the first threshold, $R' > 0$, $\Delta\tau > 0$, and τ begins to grow. As it continues to travel outward, both τ and the number of Landau levels available for pair production j_{max} and k_{max} increase. Depending on the local magnetic field strength [Eq. (11)], the photon may reach a large enough optical depth ($\tau \sim 1$) for pair production after crossing only a few thresholds (so that j_{max} and k_{max} are small) or after crossing many thresholds (so that j_{max} and k_{max} are very large). For “weak” magnetic fields ($\beta_Q \lesssim 0.1$) the optical depth increases slowly with s_{ph} and it is valid to use the $j_{\text{max}}, k_{\text{max}} \gg 1$ asymptotic attenuation coefficient for pair production (e.g., Erber 1966),

$$R'_{\parallel, \perp} \simeq \frac{0.23}{a_0} \beta_Q \exp\left(-\frac{4}{3x\beta_Q}\right), \quad (26)$$

which applies for both polarizations. For stronger fields, however, pairs are produced in low Landau levels, and the more accurate coefficients of Daugherty & Harding must be used. In Appendix B2 we find that the critical magnetic field strength separating these two regimes is

$$B_{\text{crit}} \simeq 3 \times 10^{12} \text{ G} \quad (27)$$

[see Eq. (B17)]. We also find that the boundary between the two regimes is very sharp: pairs are either created at the first few Landau levels ($n \leq 2$) for $B \gtrsim B_{\text{crit}}$ or in very high Landau levels for $B \lesssim B_{\text{crit}}$, with very few electrons/positrons

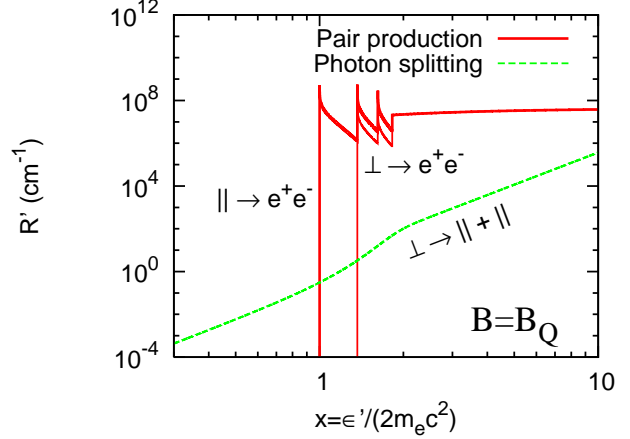


Figure 5. Attenuation coefficients in the perpendicular frame (the frame where the photon is traveling perpendicular to the magnetic field), for both photon splitting, labeled by $\perp \rightarrow \parallel + \parallel$, and pair production, labeled by $\parallel \rightarrow e^+e^-$ and $\perp \rightarrow e^+e^-$. The local magnetic field strength is $B = B_Q \simeq 4.414 \times 10^{13} \text{ G}$.

created in intermediate Landau levels. Therefore, in our simulation we only consider the first three attenuation coefficients for \parallel -polarized photons ($R'_{\parallel,00}, R'_{\parallel,01}, R'_{\parallel,02}$) and the first two non-zero attenuation coefficients for \perp -polarized photons ($R'_{\perp,01}, R'_{\perp,02}$). If the photon reaches the threshold for the (03) or (11) channel [whichever is reached first; see Eq. (25)], we use the asymptotic formula, Eq. (26). The total attenuation coefficient for pair production (as given by this approximation) is plotted in Fig. 5 for both \parallel and \perp polarizations at $\beta_Q = 1$.

We include photon splitting in our simulations. Based on the kinetic selection rule (Adler 1971; Usov 2002, but see Baring & Harding 2001), only the process $\perp \rightarrow \parallel \parallel$ is allowed. Therefore, for \parallel -polarized photons, the attenuation coefficient for photon splitting is zero ($R'_{\parallel}^{\text{sp}} = 0$). For \perp -polarized photons we use the following formula, adapted from the numerical calculation of Baring & Harding (1997):

$$R'_{\perp \rightarrow \parallel \parallel}^{\text{sp}} \simeq \frac{\frac{a_f^2}{60\pi^2 a_0} \left(\frac{26}{315}\right)^2 (2x)^5 \beta_Q^6}{[g(\beta_Q, x) + 0.05][0.25g(\beta_Q, x) + 20]}, \quad (28)$$

where $g(\beta_Q, x) = \beta_Q^3 \exp(-0.6x^3)$. For $x \leq 1$, this expression reproduces the results of Baring & Harding to better than 10% at both $\beta_Q \leq 0.5$ and $\beta_Q \gg 1$, while underestimating the results at $\beta_Q = 1$ by less than 30%. The $\perp \rightarrow \parallel \parallel$ attenuation coefficient for photon splitting is plotted in Fig. 5 at $B = B_Q$. Because the attenuation coefficient $R'_{\perp \rightarrow \parallel \parallel}^{\text{sp}}$ drops rapidly with field strength for $\beta_Q < 1$, photon splitting is unimportant for $\beta_Q \lesssim 0.5$ (e.g., Baring & Harding 2001). However, for \perp -polarized photons propagating in superstrong fields $\beta_Q \gtrsim 0.5$, photon splitting is the dominant attenuation process: even though above the first threshold ($x \geq x_{01}$ for \perp photons) the attenuation coefficient for photon splitting is much smaller than that for pair production, in superstrong fields the photon splits before reaching the first threshold (see Fig. 5).

In the simulation, whenever $\tau \geq 1$ or $\tau_{\text{sp}} \geq 1$ the photon is destroyed (i.e., turned into a pair or two photons). More precisely, the photon should only be destroyed with probability $1 - \exp(-\tau)$. But in practice we find that such

a refinement has a negligible effect on the cascade result. If $\tau_{\text{sp}} \geq 1$ the photon splits into two. As a simplification we assume that each photon takes half of the energy of the parent photon (cf. Baring & Harding 1997); therefore, at the point of photon splitting a new photon is created with an energy $0.5\epsilon_0$ and a weighting factor $2\Delta N_\epsilon$ (i.e., the simulation photon represents two actual photons). The new photon is \parallel -polarized (for the $\perp \rightarrow \parallel$ process) and is assumed to be traveling in the same direction as the parent photon, Θ_{ph} . If $\tau \geq 1$ the photon creates an electron-positron pair. For $B \lesssim B_{\text{crit}} \sim 3 \times 10^{12}$ G, the pairs are created in high Landau levels (see above), and we assume that the electron and positron each shares half of the photon energy and travels in the same direction as the photon: thus $\gamma m_e c^2 = \epsilon/2$ and the electron/positron's magnetic pitch angle is $\Psi = \psi$. This approximation is valid as long as $x\beta_Q \lesssim 0.1$ (see Daugherty & Harding 1983), which according to ML07 is satisfied for $B \lesssim B_{\text{crit}}$. When $B \gtrsim B_{\text{crit}}$, the electron and positron are created in low Landau levels (we choose the maximum allowed values, $j_{\text{max}}, k_{\text{max}}$, since this channel dominates the total attenuation coefficient), with energies given by Eq. (B5) of Appendix B1.

In the simulation we try to find the photon-magnetic field intersection angle at which pair creation occurs, ψ_{pair} , to an error of less than 10%. If the error in ψ_{pair} is too large, the electron and positron will be created in the wrong Landau level and will emit too many or too few synchrotron photons (see Section 3.3). To accurately determine ψ_{pair} we use the following procedure in our simulation: The photon's first full step, s_0 , should be small enough that the probability of pair production is negligible at s_0 but large enough that the probability grows rapidly with subsequent steps. At high fields a good choice for s_0 is the location of the first non-zero threshold ($x = x_{00}$ for \parallel polarization or $x = x_{01}$ for \perp polarization), since the attenuation coefficients are large enough to allow pair production in a distance much shorter than 1 cm. At low fields a good choice is the point where $x\beta_Q = 1/20$. At this point the mean free path for pair production is much larger than the gap height while for $x\beta_Q = 1/10$, e.g., the mean free path is much smaller than the gap height. Therefore, s_0 is chosen such that it solves

$$x = \begin{cases} x_{00}, & \beta_Q > 1/20 \text{ and } \parallel \text{ polarization;} \\ x_{01}, & \beta_Q > 1/20 \text{ and } \perp \text{ polarization;} \\ 1/(20\beta_Q), & \beta_Q < 1/20. \end{cases} \quad (29)$$

Note that both x and β_Q depend on s_0 , so the value of s_0 must be found numerically. Since $\sin \psi \simeq s_{\text{ph}}/\mathcal{R}_c$ (for small angles), this distance is approximately given by

$$s_0 \simeq \mathcal{R}_c \frac{2m_e c^2}{\epsilon} \left(1 + \frac{1}{20\beta_Q} \right). \quad (30)$$

In our simulation, for \parallel polarizations (no photon splitting), the photon moves directly to s_0 in one step. For \perp polarizations, the photon moves to s_0 in 10 steps (with step sizes $0.1s_0$), allowing for the possibility of photon splitting before reaching this point. In either case, once the photon reaches s_0 it steps outward in the manner described at the beginning of this section. At high fields ($B \gtrsim B_{\text{crit}}$) we choose the step size to be $\Delta s_{\text{ph}} = 0.1s_0(x_{01} - x_{00})/x_{00}$ for \parallel polarizations or $0.1s_0(x_{02} - x_{01})/x_{02}$ for \perp polarizations. At low fields ($B \lesssim B_{\text{crit}}$) we choose $\Delta s_{\text{ph}} = 0.1s_0$.

Sometimes the photon does not pair produce (or split)

before exiting the magnetosphere. Conveniently, we do not have to track the photons out to the light cylinder to know whether pair production will occur. Once a photon reaches the x_{03} or x_{11} threshold, such that the asymptotic expression for pair production Eq. (26) can be used (i.e., when $B \lesssim B_{\text{crit}}$), then the growth in optical depth depends “exponentially” on $x\beta_Q$ [since $\Delta\tau \propto \exp\{-1/(x\beta_Q)\}$]. Because $x\beta_Q \propto s_{\text{ph}}(r_{0,\text{ph}} + s_{\text{ph}})^{-7/2}$ reaches a maximum at $s_{\text{ph}} \simeq 0.4r_{0,\text{ph}}$ and then rapidly decreases (cf. Hirschman & Arons 2001a), we assume in our simulation that if the photon does not pair produce by

$$s_{\text{ph,max}} = 0.5r_{0,\text{ph}}, \quad (31)$$

it will never pair produce and instead escapes the magnetosphere. Here $r_{0,\text{ph}}$ is the altitude of the photon at the emission point. Note that Eq. (31) is also approximately valid for our treatment of non-dipole fields ($\mathcal{R}_c = R$ near the stellar surface), since once the photon has traveled a distance $s_{\text{ph}} \simeq s_{\text{ph,max}}$ it is in the dipole regime ($r > 2R$).

3.3 Propagation and photon emission of the secondary electrons and positrons

3.3.1 Synchrotron radiation

In the corotating frame (the “lab” frame) the secondary electron (or positron) is created with energy $\gamma m_e c^2$, pitch angle Ψ [with the corresponding Landau level n ; see Eq. (32) below] and weighting factor ΔN_ϵ (Section 3.1). For the purpose of tracking the synchrotron emission from the electron it is easier to work in the “circular” frame, the frame in which the electron has no momentum along the magnetic field direction and only moves transverse to the field in a circular motion. Note that this frame is in general different from the perpendicular frame (defined in Section 3.2) of the progenitor photon; only if the electron-positron pair is created exactly at threshold [$x = x_{jk}$; see Eq. (24)] are the two frames the same. The energy of the electron in the circular frame, $E_\perp = \gamma_\perp m_e c^2$, is related to that in the lab frame by

$$\gamma_\perp = \sqrt{\gamma^2 \sin^2 \Psi + \cos^2 \Psi} = \sqrt{1 + 2\beta_Q n}. \quad (32)$$

Note this expression also gives a relation between γ_\perp and n ; we shall use γ_\perp and n interchangeably to refer to the electron's energy in the circular frame.

In the circular frame E_\perp is radiated away through synchrotron emission on the timescale

$$\begin{aligned} t_{\text{synch}} &\simeq \left| \frac{E_\perp}{P_{\text{synch}}} \right| = \frac{\gamma_\perp m_e c^2}{\frac{2e^2}{3c^3} (\gamma_\perp^2 - 1) c^2 \omega_c^2} \\ &\simeq 5 \times 10^{-16} B_{12}^{-2} \gamma_\perp^{-1} \text{ s}, \end{aligned} \quad (33)$$

where $\omega_c = eB/m_e c$ is the electron cyclotron frequency and B_{12} is the local magnetic field strength B in units of 10^{12} G. This decay time is much shorter than other relevant cascade timescales (e.g., the timescale for B or \mathcal{R}_c to change significantly, which is of order $r/c \gtrsim 10^{-4}$ s, or the timescale for the emission of resonant ICS photons, discussed later in this section). Therefore, in the simulation the electron is assumed to lose all of its perpendicular momentum p_\perp “instantaneously” due to synchrotron radiation, before moving from its initial position (cf. Daugherty & Harding 1982).

The final energy of the electron once it reaches the ground Landau level (or $p_{\perp} = 0$) is given by

$$\gamma_{\parallel} = (1 - \beta^2 \cos^2 \Psi)^{-1/2} = \gamma / \gamma_{\perp}, \quad (34)$$

where $\beta = \sqrt{1 - 1/\gamma^2}$ is the electron velocity.

Since the synchrotron photon may carry an energy comparable to E_{\perp} of the parent electron, it is necessary to track the electron energy after each photon is emitted in order to obtain accurate synchrotron spectrum (this is in contrast to the case of curvature radiation discussed in Section 3.1, where a large number of curvature photons can be emitted without significantly affecting the energy of the parent electron). As a simplification, in the circular frame the synchrotron photons are assumed to be emitted isotropically in the plane of motion, such that no velocity kick is imparted to the electron; thus the frame corresponding to circular motion of the electron does not change over the course of the synchrotron emission process. In other words, as the electron loses its p_{\perp} , the Lorentz factors γ and γ_{\perp} decrease but γ_{\parallel} is constant, and Eq. (34) remains valid during the entire synchrotron emission process.

We adopt the following procedure in our simulation: In the circular frame, the electron Lorentz factor γ_{\perp} drops from its initial value to $\gamma_{\perp} = 1$ in a series of steps; when $\gamma_{\perp} = 1$ (i.e., $n = 0$) synchrotron emission stops. In each step one synchrotron photon is emitted, with an energy ϵ_{\perp} that depends strongly on the ‘‘current’’ value of γ_{\perp} . After the photon is emitted the energy of the electron is reduced by the amount $\Delta\gamma_{\perp} = \epsilon_{\perp}/m_e c^2$. In the next step another photon is emitted with a new value of ϵ_{\perp} , and so on.

In the simulation the photon energy ϵ_{\perp} of the synchrotron radiation is chosen in one of three ways, depending on the Landau level number n of the electron. (i) If the electron is created in a high Landau level ($n \geq 3$), the energy of the photon is chosen randomly, but with a weighting based on the asymptotic synchrotron spectrum⁶ (e.g., Sokolov & Ternov 1968; Harding & Preece 1987)

$$\frac{d^2 N}{dt d\epsilon_{\perp}} = \frac{\sqrt{3}}{2\pi} \frac{\alpha_f \omega_c}{\epsilon_{\perp}} \times \left[f F \left(\frac{\epsilon_{\perp}}{f \epsilon_{\text{SR}}} \right) + \left(\frac{\epsilon_{\perp}}{\gamma_{\perp} m_e c^2} \right)^2 G \left(\frac{\epsilon_{\perp}}{f \epsilon_{\text{SR}}} \right) \right], \quad (35)$$

where

$$\epsilon_{\text{SR}} = \frac{3}{2} \gamma_{\perp}^2 \hbar \omega_c \quad (36)$$

is the characteristic energy of the synchrotron photons, $f = 1 - \epsilon_{\perp}/(\gamma_{\perp} m_e c^2)$ is the fraction of the electron’s energy remaining after photon emission, $F(x) = x \int_x^{\infty} K_{5/3}(t) dt$,

⁶ This expression differs from the classical synchrotron spectrum (e.g., Rybicki & Lightman 1979) in two ways: First, a factor of $f = 1 - \epsilon_{\perp}/(\gamma_{\perp} m_e c^2)$ appears in several places throughout Eq. (35); when the photon energy is equal to the electron energy ($\epsilon_{\perp} = \gamma_{\perp} m_e c^2$ or $f = 0$) the asymptotic expression goes to zero. Second, a term containing the function $G(x)$ appears in Eq. (35). While such a term appears in the classical expressions for the radiation spectra of both \parallel - and \perp -polarized photons, in the classical expression for the total radiation spectra these terms cancel out. However, when the quantum effect of the electron spin is considered there is an asymmetry between the perpendicular and parallel polarizations such that the $G(x)$ term remains.

and $G(x) = x K_{2/3}(x)$ [cf. Eq. (15)]. (ii) If $n = 2$, the energy of the photon is either that required to lower the electron to its ground state ($n = 2 \rightarrow 0$) or the first excited state ($n = 2 \rightarrow 1$), with a probability that depends on the local magnetic field strength. We do not use the exact transition rates for the $n = 2$ state here. Instead, we use the following simplified prescription, based on the results of Herold, Ruder, & Wunner (1982) (see also Harding & Preece 1987): If $\beta_Q < 1$ the energy of the photon is chosen to be that required to lower the electron to the first excited state, $\epsilon_{\perp} = m_e c^2 \left(\sqrt{1 + 4\beta_Q} - \sqrt{1 + 2\beta_Q} \right)$. If $\beta_Q \gtrsim 1$ the energy of the photon is randomly chosen to be that required to lower the electron to either the ground state [$\epsilon_{\perp} = m_e c^2 \left(\sqrt{1 + 4\beta_Q} - 1 \right)$], 50% of the time, or the first excited state, 50% of the time. (iii) If $n = 1$, the energy of the photon is that required to lower the electron to its ground state, $\epsilon_{\perp} = m_e c^2 \left(\sqrt{1 + 2\beta_Q} - 1 \right)$. If the electron is not in the ground state after emission of the synchrotron photon (which could happen for the $n = 2$ and $n \geq 3$ cases discussed above, but not for the $n = 1$ case), γ_{\perp} is recalculated and a new photon energy is chosen.

The energy of the photon is transformed from the circular frame into the ‘‘lab’’ frame using

$$\epsilon = \gamma_{\parallel} \epsilon_{\perp}. \quad (37)$$

The photon carries with it the same weighting factor ΔN_{ϵ} as the secondary particle that emitted it. Because the photon is emitted in a random direction perpendicular to the magnetic field in the circular frame, in the lab frame the angle of emission (relative to the dipole axis) is approximately given by

$$\Theta_{\text{ph}} \simeq \chi + \Psi \cos \Pi, \quad (38)$$

where Π is a random angle between 0 and 2π , χ is the angle between the local magnetic field and the dipole axis and is given by Eq. (16), and the pitch angle is given by Eqs. (32) and (34):

$$\Psi = \arcsin \left(\sqrt{\frac{\gamma_{\perp}^2 - 1}{\gamma_{\perp}^2 \gamma_{\parallel}^2 - 1}} \right). \quad (39)$$

For synchrotron radiation the polarization fraction is between 50% and 100% polarized perpendicular to the magnetic field (which is the exact opposite of the curvature radiation case; see Rybicki & Lightman 1979). Therefore we randomly assign the photon a polarization in the ratio of one \parallel to every seven \perp photons (corresponding to a 75% perpendicular polarization).

3.3.2 Resonant inverse Compton scattering

Once the electron loses all of its perpendicular momentum, it moves along the magnetic field line in a stepwise fashion while upscattering surface thermal photons through RICS. The step size Δs is related to ΔN_{RICS} , the number of photons scattered in each step, by

$$\Delta s \simeq \frac{c \Delta N_{\text{RICS}}}{dN_{\text{RICS}}/dt}. \quad (40)$$

In our simulation we choose ΔN_{RICS} to be

$$\Delta N_{\text{RICS}} = \min \left(1, 0.1R \frac{dN_{\text{RICS}}/dt}{c} \right). \quad (41)$$

In other words, $\Delta N_{\text{RICS}} = 1$ if the RICS process is efficient enough to produce at least one resonant photon within a distance of $0.1R$; otherwise ΔN_{RICS} is chosen so that the electron step size is $\Delta s = 0.1R$. Using Eq. (A6) from Appendix A, we have

$$\Delta s \simeq \frac{\Delta N_{\text{RICS}}}{\left[\frac{\beta_Q}{\gamma_{\parallel}^2 \beta_{\parallel} a_0} \left(\frac{kT}{m_e c^2} \right) \ln \frac{1 - e^{-\epsilon c / [\gamma_{\parallel} (1 - \beta_{\parallel}) kT]}}{1 - e^{-\epsilon c / [\gamma_{\parallel} (1 - \beta_{\parallel} \cos \psi_{\text{crit}}) kT]}} \right]}, \quad (42)$$

where $\beta_{\parallel} = \sqrt{1 - 1/\gamma_{\parallel}^2}$ is the speed of the electron after it has completed synchrotron emission (so that $p_{\perp} = 0$), and ψ_{crit} is the incidence angle with respect to the electron's trajectory of photons coming from the edge of the surface "hot spot" (see Fig. A1). The mean energy of the scattered photons is (e.g., Beloborodov & Thompson 2007)

$$\epsilon = \gamma_{\parallel} \left(1 - \frac{1}{\sqrt{1 + 2\beta_Q}} \right) m_e c^2, \quad (43)$$

and the energy loss of the electron in each step is given by

$$\Delta \gamma_{\parallel} m_e c^2 = -\epsilon \Delta N_{\text{RICS}}. \quad (44)$$

In the lab frame the photon's angle of emission is approximately given by

$$\Theta_{\text{ph}} \simeq \chi + \frac{1}{\gamma_e} \cos \Pi, \quad (45)$$

where Π is a random angle between 0 and 2π and χ is the angle between the local magnetic field and the dipole axis [Eq. (16)]. Here, γ_e is the final Lorentz factor of the electron after emitting the photon; from Eq. (43), its value is approximately

$$\gamma_e \simeq \frac{\gamma_{\parallel}}{\sqrt{1 + 2\beta_Q}}. \quad (46)$$

While we include the $1/\gamma_e \cos \Pi$ term in Eq. (45) for completeness, we find that it is not important for our simulation. This is true even at $B \gtrsim B_Q$, where γ_e is much smaller than the initial Lorentz factor of the electron and pair production can occur almost immediately after the photon is scattered (Beloborodov & Thompson 2007). The extra distance traveled by the photons in order to pair produce when the photons are upscattered tangent to the local magnetic field (i.e., when $\Theta_{\text{ph}} = \chi$ is assumed) has a negligible effect on the overall cascade.

In the superstrong field regime, the final polarization state of a photon upscattered through RICS is given by the results of Gonthier et al. (2000). For $B \lesssim B_Q$, both below and above resonance more \perp photons are produced than \parallel photons, at a ratio of $\simeq 3 : 1$. The same situation occurs for $B \gtrsim B_Q$ below resonance; above resonance, however, the situation reverses and more \parallel photons are produced than \perp photons. We therefore assign the photons a polarization in the ratio of one \parallel to every three \perp photons for $B < B_Q$, and a polarization in the ratio of one \parallel to every \perp photon for $B \geq B_Q$ (based on the assumption that approximately 50% of the photons are slightly below resonance and 50% are slightly above). In practice, however, we find that the cascade does

not depend sensitively on the initial photon polarization. At low fields ($B \lesssim 3 \times 10^{12}$ G) the polarization has no effect on the cascade, since the asymptotic attenuation coefficient for pair production is used; at high fields a \perp photon is split into two \parallel photons before it can pair produce, and the resulting cascade is not much different from the cascade of a single \parallel photon with twice the energy.

In our simulation we consider thermal photon emission from three types of surface "hot spots" (see Pons et al. 2007 for a review of neutron star surface temperatures in strong magnetic fields): a large cool spot, $T_6 = 0.3$ and $\theta_{\text{spot}} = \pi/2$, representing emission from the entire surface of a neutron star; a mid-sized warm spot, $T_6 = 1.0$ and $\theta_{\text{spot}} = 0.3$; and a small hot spot, $T_6 = 3.0$ and $\theta_{\text{spot}} = 0.1$, representing emission from a heated polar region 1 km across (which, though small, is still significantly larger than the polar cap region, unless $P \leq 0.01$ s). We also consider the case where ICS has no effect on the cascade, which we find occurs for $T_6 \lesssim 0.1$ (neutron stars too cold), $\theta_{\text{spot}} \lesssim 0.01$ (hot spots too small), or $r_0 \gtrsim R(1 + 2\theta_{\text{spot}})$ (particles injected too far away from the surface; this is most relevant for photon-initiated cascades discussed in Section 3.4 below).

3.4 Cascades initiated by a primary photon

In the second version of the simulation, a photon is created with energy ϵ_0 at the position $(r_{0,\text{ph}}, \theta_{0,\text{ph}})$. We typically choose $r_{0,\text{ph}} = R$ and $\theta_{0,\text{ph}} = \theta_{\text{cap}}$ (cf. Section 3.1), since the resonant ICS photon density is largest at $r \simeq R$; however, we are also interested in photons emitted at a higher altitude (e.g., for surface field strengths $B_p \gtrsim 10^{13}$ G the behavior of the cascade with $r_{0,\text{ph}} = R$ and with $r_{0,\text{ph}} = 3R$ are very different; see Section 4). We set $\Delta N_{\epsilon} = 1$, such that each photon in the simulation represents exactly one photon in reality; we can later multiply the simulation results by N_0 of Eq. (9) if we wish to compare cascades dominated by RICS and by curvature radiation (see Section 2.2). The photon is injected tangent to the magnetic field [$\Theta_{\text{ph}} = \chi$; cf. Eq. (17)], since we find almost no difference in the final photon or pair spectra if we add a beaming angle $1/\gamma \sim 10^{-7} - 10^{-3}$. As was discussed in Section 3.3.2, resonant ICS photons have a polarization ratio \parallel to \perp of approximately 1:3 for $B < B_Q$ and approximately 1:1 for $B \geq B_Q$. In Section 4.1, results for the photon-initiated cascades, we choose the initial photon to be polarized perpendicular to the magnetic field, to create a cascade with particle multiplicities as large as possible. Our results therefore represent upper bounds on the actual cascade multiplicities. The actual cascade should not differ greatly from that presented in Section 4.1, however, as cascades initiated by photons polarized parallel to the magnetic field are only slightly lower in particle multiplicity and are qualitatively similar in spectral shape. Once the initial parameters of the photon have been chosen, the simulation proceeds in the exact same way as described in Sections 3.2–3.3: the photon steps outward in a straight line from the point of emission until its optical depth is large enough to pair produce or split, etc.

Note that due to the discrete, random nature of the synchrotron emission and the small number of particles involved in the cascade, photon-initiated cascades will have photon and pair spectra that are coarse and that vary between simulation runs. In order to smooth/average the spec-

tra to some extent, we modify the synchrotron emission procedure of Section 3.3 for secondary particles in high Landau levels ($n \geq 3$). In every step 10 photons are emitted, each with a weighting factor of $0.1\Delta N_\epsilon$ (rather than one photon with a weighting factor of ΔN_ϵ , as before). Each photon has a different energy $\epsilon_{\perp,i}$ [chosen randomly according to Eq. (35)], so that the total energy lost by the secondary particle becomes $\gamma_\perp m_e c^2 = 0.1 \sum_{i=1}^{10} \epsilon_{\perp,i}$. We do not apply this procedure to the synchrotron emission from secondary particles in Landau levels $n = 1$ or $n = 2$, as it would not gain anything; each of the 10 photons emitted would have the same value of $\epsilon_{\perp,i}$.

4 RESULTS

In this section we present the results of our simulations of photon- and electron-initiated cascades (Sections 4.1 and 4.2, respectively), for a variety of different surface field strengths, rotation periods, field geometries, and initial energies of the primary particle. For each type of cascades, we present the “final” spectra of the cascade photons and pairs as they cross the light cylinder and escape from the magnetosphere. For the electron-initiated cascades we also show the spectra at several intermediate stages (i.e., the spectra of all photons and pairs that cross the height $r = 1.2R, 2R, 5R$, etc.). The photon spectra are plotted over the energy range 10 keV–1 TeV, since for energies $\lesssim 1$ keV the thermal photons dominate the spectra while above ~ 1 TeV fewer than one photon is produced per primary electron. We are particularly interested in the pair multiplicities, i.e., the total number of cascade electrons + positrons produced per primary particle. We use n_E to denote the number of electrons and positrons per “primary” photon and N_E to denote the number per primary electron; the two multiplicities are related by

$$N_E = N_0 \times n_E, \quad (47)$$

where N_0 is the number of photons produced by the primary electron (see Section 2.2). From our numerical results we infer various empirical relations for each cascade; quantitative arguments for the validity of several of these relations are given in Appendix C.

We first present our results for photon-initiated cascades (see Section 3.4), as they are simpler and aid us in our discussion of the results for the full cascade (initiated by a primary electron).

4.1 Results: photon-initiated cascades

Our results for photon-initiated cascades are presented in Figs. 6–9. We consider primary photons with energies in the range of 10^3 – 10^5 MeV; for $B_{p,12} = 1$ –1000, the primary electron should emit very few photons (via either resonant ICS or curvature radiation) above this energy range (see Section 2). Unless otherwise stated, the primary photon is emitted from near the surface, in the direction tangent to the last open field line. Thus the radius of curvature near the point of emission is $\mathcal{R}_c \simeq 9 \times 10^7 P_0^{1/2}$ cm for dipole fields [Eq. (14)].

We find significant differences in the behavior of the cascades at magnetic field strengths below and above

$B_{\text{crit}} \simeq 3 \times 10^{12}$ G [Eq. (B17)]. At low fields $B \lesssim B_{\text{crit}}$, the primary photon can pair produce if [Eq. (C2)]; see also Hibschan & Arons 2001a]

$$\epsilon_0 > \epsilon_{\text{min}} \sim 3000 B_{p,12}^{-1} \mathcal{R}_8 \text{ MeV}, \quad (48)$$

where \mathcal{R}_8 is the radius of curvature \mathcal{R}_c in units of 10^8 cm, evaluated at the surface along the last open field line. Strong cascades, where more than one electron-positron pair is produced, typically occur at energies ~ 10 times ϵ_{min} . For ϵ_0 in the range from ϵ_{min} to $\sim 10^5$ MeV, we find that the multiplicities of photons and e^+e^- particles produced in the cascade are

$$n_\epsilon \sim \frac{\epsilon_0}{500 \text{ MeV}} \mathcal{R}_8^{-1} \quad (49)$$

and

$$n_E \sim \frac{\epsilon_0}{10^4 \text{ MeV}} B_{p,12} \mathcal{R}_8^{-1}, \quad (50)$$

respectively. These results are (largely) independent of the hot spot model used. When ICS is inactive, the cascade electron/positron has final energy (after it has finished radiating synchrotron photons) extending from [Eq. (C3)]

$$E_{\text{max}} \sim 0.1 B_{p,12} \epsilon_0 \quad (51)$$

(for the first pair produced) down to $\sim 0.1 B_{p,12} \epsilon_{\text{min}}$ for the lowest-energy pairs, and the total energy of the pairs is [Eq. (C4)]

$$\mathcal{E}_{\text{tot}} \sim 2E_{\text{max}} + 0.1 B_{p,12} \epsilon_{\text{min}} n_E \ln \left(\frac{0.075 \epsilon_0}{\epsilon_{\text{min}}} \right). \quad (52)$$

When ICS is active from a hot spot (Section 3.3), the number of pairs produced does not change, since the photons produced through ICS at these field strengths have energies $\sim B_{p,12}^2 T_6^{-1}$ MeV [Eq. (8)] and can not pair produce. The total pair energy \mathcal{E}_{tot} decreases, however, since the ICS process transfers energy from the pairs to photons. Although resonant ICS is most important for electrons and positrons at $\gamma_{\text{crit}} \simeq \epsilon_c/kT$ [Eq. (7); see Section 2.2], we find in these cascades that all electrons and positrons with energies in the range of

$$\begin{aligned} E_{\text{RICS}} &\sim (0.3 - 30) \gamma_{\text{crit}} m_e c^2 \\ &\simeq (20 - 2000) B_{p,12} T_6^{-1} \text{ MeV} \end{aligned} \quad (53)$$

are strongly affected. Thus hot surface spots with higher T tend to lower \mathcal{E}_{tot} more. As expected, we find that photon splitting does not affect the cascade at these field strengths (see Section 3.2). The photon and pair cascade spectra for $B_{p,12} = 1$ are shown in Fig. 6, both when ICS is inactive and when ICS is active from a “warm spot” ($T_6 = 1, \theta_{\text{spot}} = 0.3$).

At high fields ($B \gtrsim B_{\text{crit}}$), a primary photon injected from the surface will pair produce when

$$\epsilon_0 > \epsilon_{\text{min}} \sim 200 \mathcal{R}_8 \text{ MeV}, \quad (54)$$

largely independent of field strength. When ICS is inactive, almost all of the cascade energy resides in the pairs; i.e., $\mathcal{E}_{\text{tot}} \simeq \epsilon_0$. The pair cascade will be very weak regardless of photon energy, with $n_E < 10$ and $n_\epsilon = 0$ or 1 (i.e., at most one photon escapes the magnetosphere without pair production). This is because the e^\pm pairs are produced exclusively through the $(jk) = (00)$ or (01) channel (see Section 3.2), so that at most one synchrotron photon is emitted per pair. For $B_{p,12} \gtrsim 20$, photon splitting causes all pairs to be produced

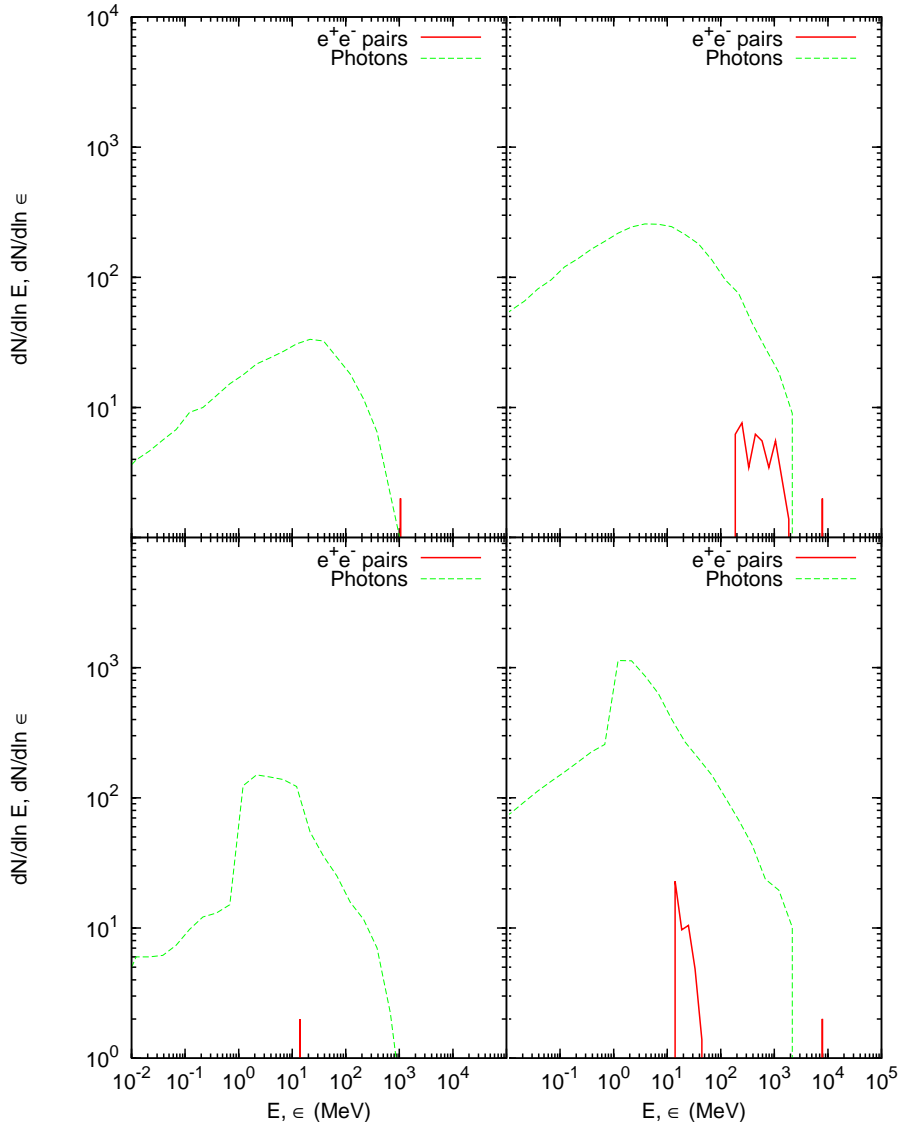


Figure 6. The final photon and pair spectra of photon-initiated cascades for surface magnetic fields $B_{p,12} = 1$. The NS spin period is $P_0 = 1$ and a dipole field geometry is adopted. In the upper panels, ICS is assumed to be inactive, while in the lower panels, ICS from a hot spot with $T_6 = 1$, $\theta_{\text{spot}} = 0.3$ is included in the simulation. The primary photon is injected from the surface and has an energy of 10^4 MeV (left panels) or 10^5 MeV (right panels); for photons with energy 10^3 MeV, no cascade is initiated. The spike in the pair spectra of each panel represents the electron-positron pair produced by the primary photon. The spectra in the top panels (where ICS is inactive) are nearly identical to the spectra generated, e.g., by a photon injected at $r_{0,\text{ph}} = 3R$ above a star with surface field $B_{p,12} = 3^3 = 27$, such that the local field strength at the injection point is $B = 10^{12}$ G [Eq. (11)].

with $(jk) = (00)$, such that the cascades are even weaker: $n_E \leq 4$ and $n_\epsilon = 0$. When ICS is active, both n_ϵ and n_E can be larger, though not as large as would be predicted by an extrapolation of Eqs. (49) and (50) to high fields. In order for ICS to affect the cascade, however, the primary photon must have an energy

$$\epsilon_0 \gtrsim 70 B_{p,12} T_6^{-1} \text{ MeV}; \quad (55)$$

the energy of the electron/positron produced by this photon, $E_{\text{max}} \sim (0.1-0.5)\epsilon_0$ [Eq. (C9)], must be larger than the minimum energy at which ICS is effective, $\sim 0.3\gamma_{\text{crit}}m_e c^2$ (see Appendix C1). Note that this energy is approximately equal

to ϵ_{RICS} , the energy of a typical ICS photon upscattered by the primary electron at high fields [Eq. (8)]; therefore, at high fields a typical ICS photon is able to initiate a weak cascade. We find that for $B_p \lesssim 0.5B_Q$ a significant fraction ($\sim 20\%-60\%$) of the total cascade energy ϵ_0 resides in the photons; as in the low field case [Eq. (52)], this fraction decreases as either ϵ_0 or $B_{p,12}$ increases. For $B_p \gtrsim 0.5B_Q$, even ignoring photon splitting, the total photon energy fraction is very low, $< 10\%$; but with photon splitting included, it is almost negligible, $< 1\%$. The photon and pair cascade spectra for $B_{p,12} = 10$ and 100 when ICS is active from a “warm spot” ($T_6 = 1$, $\theta_{\text{spot}} = 0.3$) are shown in Fig. 7.

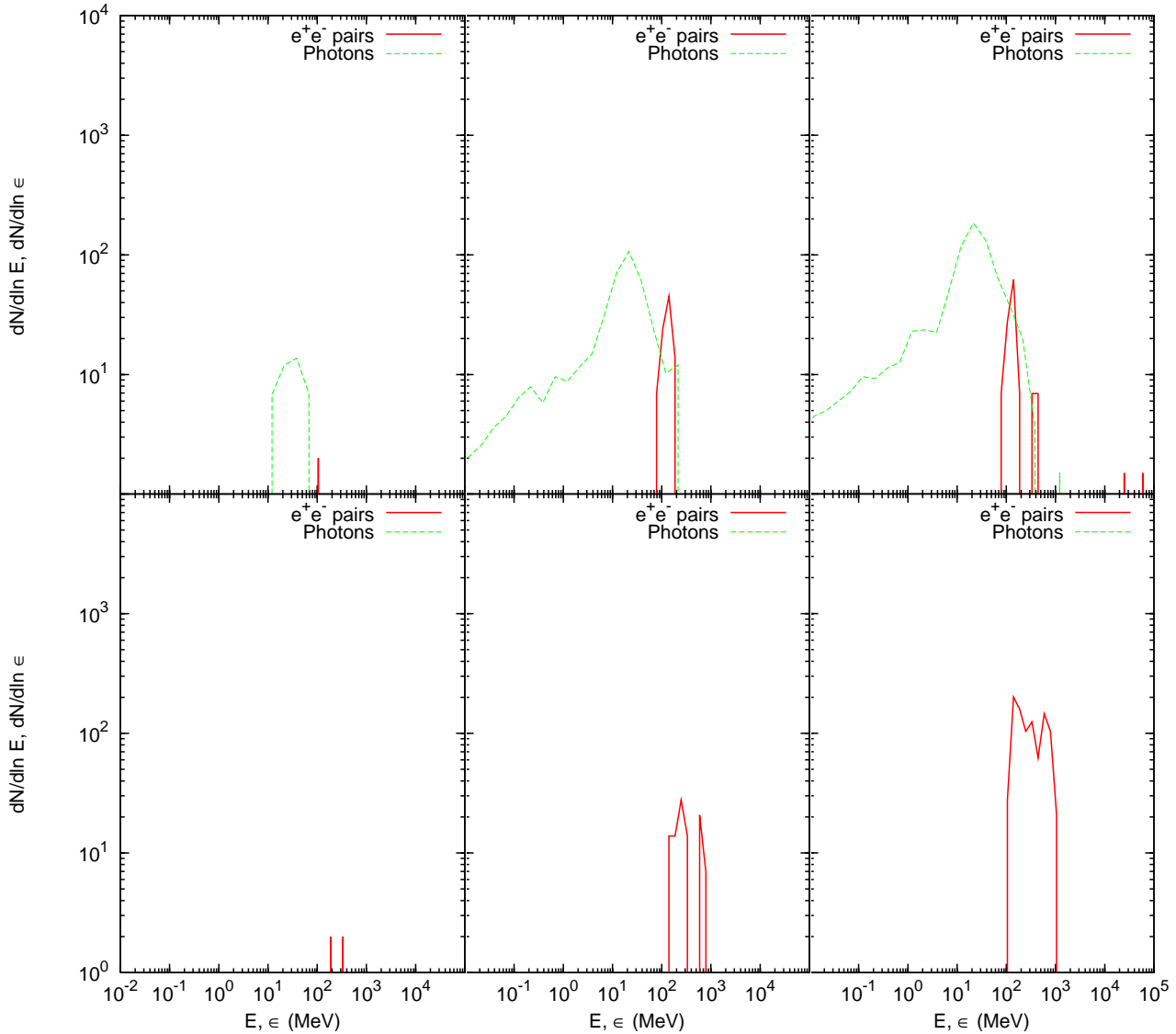


Figure 7. The final photon and pair spectra of photon-initiated cascades with active ICS, for surface magnetic fields $B_{p,12} = 10$ (upper panels) and 100 (lower panels). The pulsar spin period is $P_0 = 1$, a dipole field geometry is adopted, photon splitting $\perp \rightarrow \parallel$ is active, and thermal photons are emitted from a hot surface spot with $T_6 = 1$, $\theta_{\text{spot}} = 0.3$. The primary photon has an energy of 10^3 MeV (left column of panels), 10^4 MeV (middle column), or 10^5 MeV (right column). The spikes in the pair spectra of several panels represent the electron-positron pair produced by the primary photon. Note that there are actually two such pairs in the bottom left panel ($B_{p,12} = 100$, $\epsilon_0 = 10^3$ MeV), as the primary photon has split in that case; while in the upper right panel ($B_{p,12} = 10$, $\epsilon_0 = 10^5$ MeV) the electron and positron have significantly different energies from each other and so are represented by two shorter spikes. Also note that photon spectra do not appear in the lower panels. This is due to a combination of weak synchrotron emission and efficient pair production near the surface of a $B_{p,12} \geq 100$ neutron star; very few secondary photons are created, and none of them survive to escape the magnetosphere.

As discussed in Section 3.3, we consider three hot surface spot models for active ICS: a “cool” $T_6 = 0.3$, $\theta_{\text{spot}} = \pi/2$ spot; a “warm” $T_6 = 1$, $\theta_{\text{spot}} = 0.3$ spot; and “hot” $T_6 = 3$, $\theta_{\text{spot}} = 0.1$ spot. At low fields we find that the only effect the various hot spot models have is to lower \mathcal{E}_{tot} relative to the total cascade energy ϵ_0 (see above). At high fields, the cascades due to warm and hot spots are similar in multiplicities n_e and n_E for energies $\epsilon_0 \lesssim 10^4$ MeV; but for energies $\epsilon_0 \gtrsim 10^5$ MeV, the hot spots give multiplicities ~ 3

times larger than warm spots; see Fig. 8 [from Eq. (55), at $B_{p,12} = 1000$ a strong cascade requires $T_6 \geq 3$]. Cool spots give much smaller multiplicities (factors of > 10 smaller) than warm or hot spots regardless of the primary photon energy.

At low fields, the multiplicities of photons and e^+e^- particles produced per primary photon, n_e and n_E , depend on \mathcal{R}_c to the (-1) power [Eqs. (49) and (50)], such that cascades in non-dipole magnetospheres can be much larger

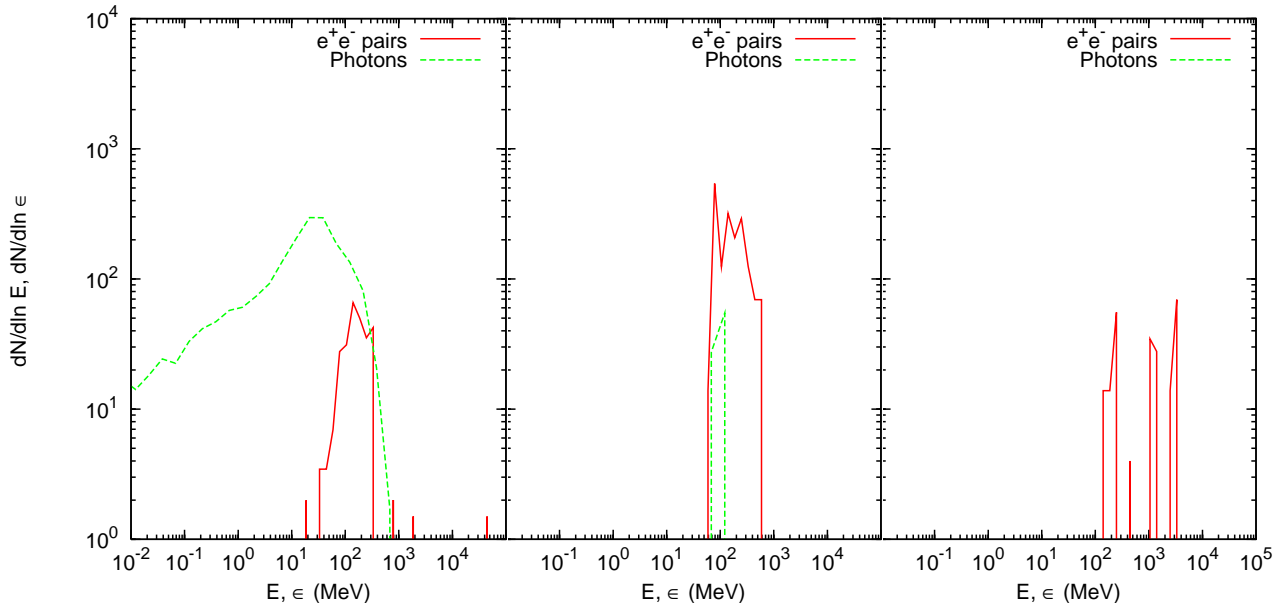


Figure 8. The final photon and pair spectra of photon-initiated cascades with active ICS, for surface magnetic fields $B_{p,12} = 10$ (left panel), 100 (middle panel), and 1000 (right panel). The NS period is $P_0 = 1$, a dipole field geometry is adopted, and thermal photons are emitted from a hot spot with $T_6 = 3$, $\theta_{\text{spot}} = 0.1$. The primary photon has $\epsilon_0 = 10^5$ MeV. The spikes in the pair spectra of the left and right panels represent, from shortest to tallest, one, two, or four electrons/positrons.

than in dipole magnetospheres. At high fields, we find that this dependence on curvature radius is much weaker: $n_E \propto \mathcal{R}_c^{-1/2}$ at $B_p \simeq 0.5B_Q$ and $n_E \propto \mathcal{R}_c^{-1/4}$ power at larger fields. Thus for high fields, the cascades in non-dipole and dipole magnetospheres are of similar sizes. The photon and pair cascade spectra for $B_{p,12} = 1, 10, \text{ and } 100$ and a $\mathcal{R}_c = R$ non-dipole magnetosphere are shown in Fig. 9.

Two aspects of the cascade depend strongly on the altitude ($r_{0,\text{ph}}$) at which the primary photon is injected: the local magnetic field strength, $B \propto r^{-3}$, and the effectiveness of ICS, which is completely negligible for $r_{0,\text{ph}} \geq 3R$ (regardless of the temperature and size of the hot spot). The other cascade parameters have a much weaker dependence on altitude (e.g., radius of curvature $\mathcal{R}_c \propto \sqrt{r_{0,\text{ph}}}$). We find that the photon and pair spectra for primary photons injected at $r_{0,\text{ph}} > R$ are very similar to the spectra for photons injected at the surface, as long as ICS is inactive and the local magnetic field strengths are the same in both cases. For example, the spectra for $r_{0,\text{ph}} = 3R$ and $B_{p,12} = 27$ [such that the local field strength at the point of injection is $B_{12} = 1$; Eq. (11)] is nearly identical to the spectra given in the first row of Fig. 6, where $r_{0,\text{ph}} = R$, $B_{p,12} = 1$, and ICS is inactive.

We can use the pair multiplicity per primary photon, $n_E(\epsilon_0)$, obtained from our numerical simulations to estimate the pair multiplicity per primary electron, $N_E = N_0 n_E$, when ICS is the dominant cascade emission process. For ϵ_0 and N_0 , we use the expressions for the typical energy ϵ_{RICS} and total number $\simeq 10B_{p,12}^{-1}P_0^{3/4}T_6^{5/2}$ of resonant ICS photons upscattered by the primary electron [Eqs. (8) and (9); see Section 2.2]. The results are shown in Table 1. Note that although ϵ_{RICS} is independent of the acceleration model used, the number of upscattered photons, N_0 , as given by Eq. (9) is applicable for only inner gap accelerators with

space-charge-limited flow; inner vacuum gap accelerators, for example, would yield N_0 about 20–100 times lower. Also note that, for a given acceleration model, an accurate determination of N_E requires that rather than just setting $\epsilon_0 = \epsilon_{\text{RICS}}$, a distribution of energies be used which takes into account resonant (and possibly non-resonant) scattering away from the thermal peak (i.e., $\gamma \neq \gamma_{\text{crit}}$): although fewer photons are upscattered at energies greater than ϵ_{RICS} , these photons can have an important effect on the total multiplicity of pairs produced, since n_E grows approximately linearly with photon energy ϵ_0 ; the $\epsilon_0 > \epsilon_{\text{RICS}}$ photons are especially important for cascades where $n_E(\epsilon_{\text{RICS}}) = 0$ (e.g., cascades with $B_{p,12} = 10$ and $P_0 = 1$).

4.2 Results: electron-initiated cascades

Our results for electron-initiated cascades are presented in Table 2 and Figs. 10–15. In our simulation, the primary electron is emitted from the surface along the last open field line ($\theta_0 = \theta_{\text{cap}}$). We consider the cases of $\gamma_0 = 2 \times 10^7$ and 4×10^7 in dipole magnetospheres, as well as the case of $\gamma_0 = 2 \times 10^6$ in non-dipole $\mathcal{R}_c = R$ magnetospheres, as discussed in Section 2.1. Although a larger initial primary energy γ_0 gives rise to more cascade particles with a larger total energy, the behavior of the cascade at $\gamma_0 > 4 \times 10^7$ is qualitatively similar to that at $\gamma_0 = (2\text{--}4) \times 10^7$ (or $\gamma_0 = 2 \times 10^6$ and $\mathcal{R}_c = R$) and key quantities such as cascade multiplicities and energies can be extrapolated from our results. For most of this section we “turn off” ICS in our simulation and allow photon splitting only through the $\perp \rightarrow \parallel \parallel$ mode; at the end of this section we discuss how changing these simulation parameters affects the cascade.

In Table 2 we list some key quantitative results of our simulations: For each cascade (characterized by the spin pe-

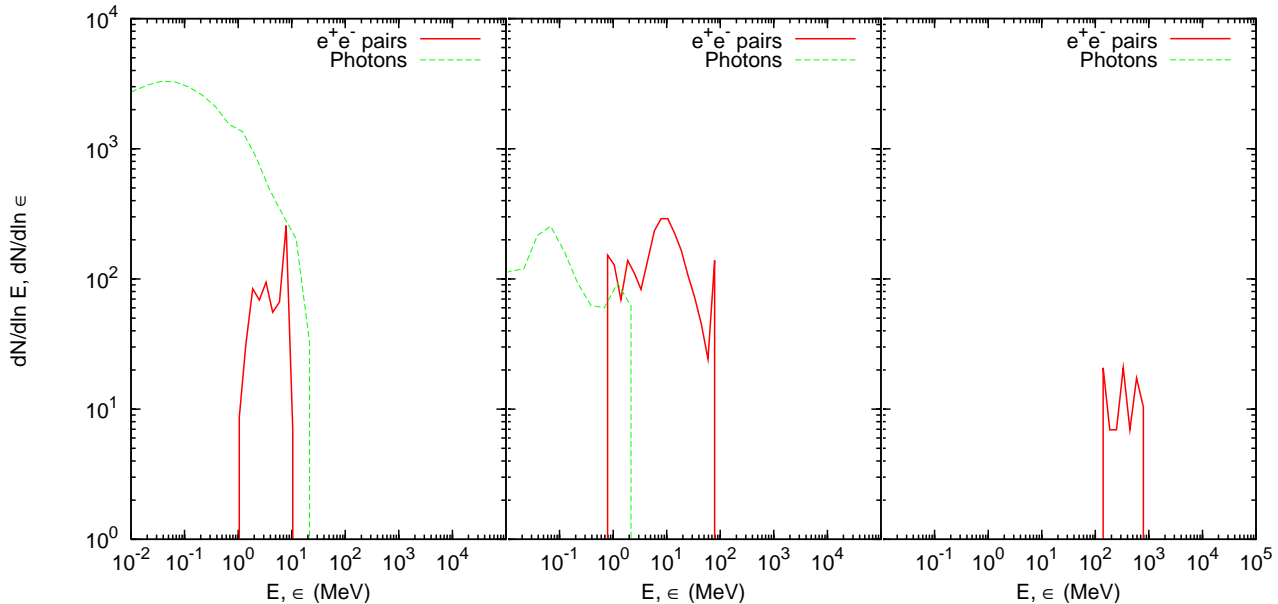


Figure 9. The final photon and pair spectra of photon-initiated cascades for a non-dipole magnetosphere with local radius of curvature $\mathcal{R}_c = R$, for surface magnetic fields $B_{p,12} = 1$ (left panel), 10 (middle panel), and 100 (right panel). Here, the primary photon has $\epsilon_0 = 10^4$ MeV and ICS is active from a hot spot with $T_6 = 1$, $\theta_{\text{spot}} = 0.3$.

Table 1. Pair multiplicity N_E when resonant ICS is the dominant photon emission process of the primary electron. For simplicity, all photons are assumed to be upscattered from the thermal peak (γ_{crit} ; see text). Each entry in the table gives $N_E = N_0 n_E$ for a different surface magnetic field strength B_p , radius of curvature (either $\mathcal{R}_c = R$ or a dipole field curvature with the pulsar spin period P_0 is specified), and hot spot temperature T and size θ_{spot} . The pair multiplicity is zero for $B_{p,12} = 1$ and the hot spot models used here, even when $\mathcal{R}_c = R$; we therefore omitted these entries from the table.

	$T_6 = 1, \theta_{\text{spot}} = 0.3$			$T_6 = 3, \theta_{\text{spot}} = 0.1$		
	$P_0 = 10$	$P_0 = 1$	$\mathcal{R}_c = R$	$P_0 = 10$	$P_0 = 1$	$\mathcal{R}_c = R$
$B_{p,12} = 10$	0	0	14	0	0	220
$B_{p,12} = 100$	2.2	1.2	1.2	35	6.2	31
$B_{p,12} = 1000$	0.7	0.1	0.1	11	1.9	4.4

riod for dipole fields or the curvature radius for multipole fields, the surface field strength B_p and the primary electron energy $\gamma_0 m_e c^2$, we give $\gamma_f m_e c^2$ (the final energy of the primary electron when it escapes the light cylinder), \mathcal{E}_{tot} (the total energy of the cascade photons), \mathcal{E}_{tot} (the total energy of the secondary e^+e^- pairs), and N_E (the multiplicity of e^+e^- pairs produced per primary electron). Note that the total cascade energy must satisfy $\gamma_0 m_e c^2 = \gamma_f m_e c^2 + \mathcal{E}_{\text{tot}} + \mathcal{E}_{\text{tot}}$. We find that N_E is largest for cascades with strong surface fields, short rotation periods, multipole geometries, or large initial energies for the primary electron, but that regardless of cascade parameters the particle multiplicity saturates at $N_E \sim 10^4$. Increasing B_p or γ_0 , or decreasing P or \mathcal{R}_c , tends to increase the ratio $f_E = \mathcal{E}_{\text{tot}}/(\mathcal{E}_{\text{tot}} + \mathcal{E}_{\text{tot}})$; i.e., under these conditions a larger fraction of the “secondary” energy, $\gamma_0 m_e c^2 - \gamma_f m_e c^2$, is transferred from the photons to the pairs. At low fields only a small fraction of the secondary energy is held by the secondary pairs (e.g., for $B_{p,12} = 1$, $f_E \lesssim 0.05$), but at high fields this fraction is typically above 50% (e.g., for $B_{p,12} = 1000$, $f_E \gtrsim 0.8$). The average energy

of a secondary electron/positron, $\bar{E} = \mathcal{E}_{\text{tot}}/N_E$, is directly proportional to the total cascade energy (i.e., $\bar{E} \propto \gamma_0$), but depends only weakly on B_p , P , and \mathcal{R}_c (e.g., \bar{E} is approximately the same for $\mathcal{R}_c = R$ and $\gamma_0 = 2 \times 10^7$ as in the dipole case for $\gamma_0 = 2 \times 10^7$).

Figure 10 shows the secondary pair multiplicities N_E as a function of γ_0 , for various field strengths and periods/field geometries. We find that for dipole geometries N_E is a strong function of both γ_0 and the ratio $B_p P^{-2}$ (i.e., the polar cap voltage), but depends very weakly on either P or B_p alone. For example, the N_E versus γ_0 curves for $B_{p,12} = 1, P_0 = 1$ and $B_{p,12} = 100, P_0 = 10$ are nearly the same, as is shown in Fig. 10. Assuming that a dense secondary pair plasma is a necessary ingredient in pulsed radio emission from neutron stars (see Section 1), we can use our pair multiplicity results to estimate the conditions for pulsar “death” — the conditions under which a NS is no longer active as a radio pulsar: For a particular set of cascade parameters B_p , P , and \mathcal{R}_c , we define γ_{death} to be the value of γ_0 at which on average only one electron/positron is created per primary electron;

Table 2. Energies and multiplicities for a cascade initiated by a single electron. Listed are the initial and final energy of the primary electron, $\gamma_0 m_e c^2$ and $\gamma_f m_e c^2$, respectively; the total energy of the cascade photons, ε_{tot} ; and the multiplicity and total and average energies of the secondary electrons and positrons, N_E , \mathcal{E}_{tot} , $\bar{E} = \mathcal{E}_{\text{tot}}/N_E$, respectively. Each cascade is specified by the magnetic field strength, field geometry (curvature radius \mathcal{R}_c or spin period in the case of dipole fields), and cascade energy ($\gamma_0 m_e c^2$).

P (1 s)	B_p (10^{12} G)	$\gamma_0 m_e c^2$ (MeV)	$\gamma_f m_e c^2$ (MeV)	ε_{tot} (MeV)	\mathcal{E}_{tot} (MeV)	N_E	\bar{E} (MeV)
10	10	1.022e7	8.1e6	2.1e6	7.4e3	1.3e1	5.7e2
	100			2.0e6	8.1e4	1.7e2	4.8e2
	1000			1.9e6	1.8e5	5.1e2	3.5e2
1	1	4.8e6	5.4e6	1.9e4	5.3e1	3.6e2	3.6e2
	10			4.9e6	5.8e5	9.6e2	6.0e2
	100			4.0e6	1.4e6	3.0e3	4.7e2
0.1	1	2.4e6	7.4e6	4.0e5	1.5e3	2.7e2	2.7e2
	10			4.4e6	3.4e6	6.0e3	5.7e2
	100			2.8e6	5.0e6	1.1e4	4.5e2
1	1	2.044e7	4.9e6	1.5e7	6.3e5	8.2e2	7.7e2
	10			9.5e6	5.9e6	3.8e3	1.6e3
	100			6.3e6	9.2e6	6.9e3	1.3e3
$\mathcal{R}_c = R$	1	1.022e6	5.8e5	3.9e5	5.2e4	6.5e3	8.0e0
	10			8.0e4	3.7e5	2.0e4	1.9e1
	100			1.3e4	4.3e5	1.9e4	2.3e1
	1000	1.5e4	4.3e5	1.8e4	4.3e5	1.8e4	2.4e1

i.e.,

$$N_E(\gamma_0 = \gamma_{\text{death}}) = 1. \quad (56)$$

The value of γ_{death} changes very little if we alter the critical value of N_E in Eq. (56) by a factor of ~ 10 , because of the steep dependence of N_E on γ_0 in this region. Therefore, although it is unknown exactly what value N_E must have for a pulsar to be active, $\gamma_0 = \gamma_{\text{death}}$ is a good predictor of pulsar death regardless. Using Fig. 10 we find empirically that

$$\gamma_{\text{death}} \simeq 1.5 \times 10^7 B_{p,12}^{-1/6} \mathcal{R}_8^{2/3}. \quad (57)$$

For dipole fields, $\mathcal{R}_8 = 0.9P_0^{1/2}$, and we can write

$$\begin{aligned} \gamma_{\text{death}} &\simeq 1.4 \times 10^7 B_{p,12}^{-1/6} P_0^{1/3} \\ &= \left(\frac{\Phi_{\text{death}}}{\Phi_{\text{cap}}} \right)^{1/6} \left(\frac{e\Phi_{\text{death}}}{m_e c^2} \right), \end{aligned} \quad (58)$$

where Φ_{cap} is given by Eq. (1) and

$$\Phi_{\text{death}} = 7 \times 10^{12} \text{ V}. \quad (59)$$

Therefore, for dipole fields, the death line is given approxi-

mately by $\Phi_{\text{cap}} = \Phi_{\text{death}}$, or

$$P_0 = B_{p,12}^{1/2}; \quad (60)$$

for $B_{p,12} = 1\text{--}1000$ this is nearly the same as the death line depicted in Fig. 1 ($P_0 = 0.6B_{p,12}^{8/15}$).

An example of how the cascades develop spatially is presented in Fig. 11, which shows the number of photons and secondary pairs as a function of the radius at which each particle is created, for surface fields strengths $B_{p,12} = 1, 44.14$ (i.e., $B_p = B_Q$), and 1000. The right two panels show the difference in the behavior of the cascade when the local magnetic field strength B is above or below $B_{\text{crit}} \simeq 3 \times 10^{12}$ G [see Eq. (27)], i.e., below or above $r \simeq 2.5R$ for $B_p = B_Q$ and $r \simeq 7R$ for $B_{p,12} = 1000$ [see Eq. (11)]. For $B \gtrsim B_{\text{crit}}$, pair production by curvature photons is very efficient; for the conditions depicted in Fig. 11 ($P_0 = 1$ and $\gamma_0 = 2 \times 10^7$) approximately one e^\pm pair is created for every two photons emitted by the primary electron. This is because about half of all the photons created at low altitudes lie above the limit $\varepsilon_{\text{min}} \sim 200$ MeV of Eq. (54) (see Fig. 14). Photon splitting has very little effect on the curvature photons, since the majority (7/8) of these photons are \parallel -polarized. There is no synchrotron radiation for $B > 0.5B_Q$, since the \parallel photons

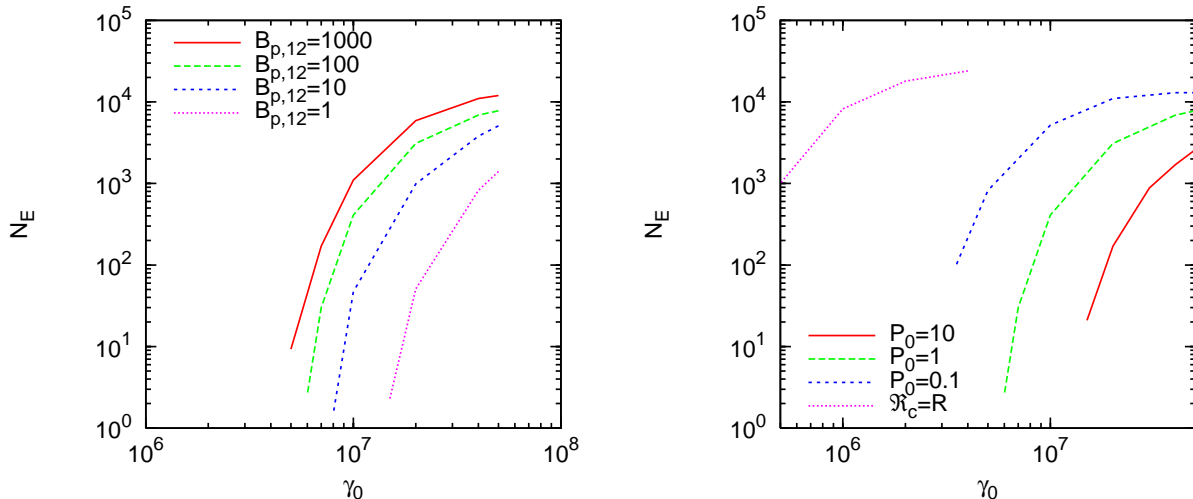


Figure 10. Secondary electron/positron multiplicities N_E as a function of the initial Lorentz factor of the primary electron γ_0 , for $P_0 = 1$ and a dipole geometry at several different surface field strengths (left panel), and for $B_{p,12} = 100$ at several different periods/field geometries (right panel).

will pair produce through the $(jk) = (00)$ channel and \perp photons will split into two \parallel photons before pair producing (see Section 3.2). For $B < 0.5B_Q$, pair production dominates over photon splitting, such that a few synchrotron photons are emitted from electrons and positrons in the $n = 1$ Landau level. For $B < B_{\text{crit}}$, electrons and positrons are created in higher Landau levels, such that many synchrotron photons are produced by each electron or positron (~ 10 ; see Appendix C1). The minimum photon energy for pair production $\epsilon_{\text{min}} \propto B^{-1}$ [Eq. (48)] grows with radius while the energy of the typical curvature photon $\epsilon_{\text{CR}} \propto \gamma^3$ [Eq. (10)] and synchrotron photon $\epsilon_{\text{SR}} \propto \epsilon_{\text{CR}}$ (Appendix C1) fall with radius; therefore the number of electron-positron pairs created per photon decreases rapidly with radius.

Figures 12 and 13 show the final spectra (i.e., the spectra as measured at the light cylinder) of photons and pairs, as well as the spectra of curvature photons emitted by the primary electron, for a variety of magnetic field strengths, spin periods, and cascade energies. Figure 14 shows cumulative photon and pair spectra at various magnetosphere radii. These spectra are generated by recording the energy of any photon, electron, or positron which reaches various radii (such as $r/R = 1.2, 2, 5, 20$).

Figures 12–14 show many of the same trends as are seen in Table 2 and Fig. 11. For example, the multiplicity N_E increases with increasing B_p , γ_0 , P^{-1} , or \mathcal{R}_c^{-1} . But there are also several new features. First, increasing B_p or γ_0 , or decreasing P or \mathcal{R}_c , tends to increase the maximum energy and decrease the minimum energy of the cascade pairs, so that the pair spectrum becomes broader in energy (see Section C2). Second, the cumulative photon and pair spectra at a given radius r (Fig. 14) are nearly independent of B_p , as long as the local field strength at that radius is larger than B_{crit} (e.g., the spectra at $r = 2R$ are nearly the same for $B_{p,12} = 44.14$ and 1000). Third, under certain conditions, synchrotron radiation dominates the cumulative/final photon spectrum at low energies $\epsilon \lesssim 1$ MeV (e.g., in the top middle and top right panels of Fig. 13): For a given alti-

tude r , the ratio of the number of synchrotron photons to the number of curvature photons at low energies is largest for large γ_0 , small P , or small \mathcal{R}_c . The ratio of synchrotron photons to curvature photons is also largest for B_p close to B_{crit} , such that the point of maximum synchrotron radiation, $B \simeq B_{\text{crit}}$ (see Fig. 11), occurs at a low altitude. Note that for $\epsilon \lesssim 0.1$ MeV the cumulative and final photon spectra all have power-law shapes with index $\Gamma = 2/3$ (where $dN/d\epsilon = \epsilon^{-\Gamma}$), regardless of whether synchrotron radiation from the secondary pairs or curvature radiation from the primary electron dominates; this is because both processes have spectra that depend on $F(x)/\epsilon \propto \epsilon^{-2/3}$ at low energies [i.e., for $x \ll 1$; see Eqs. (15) and (35)].

Figure 15 shows the effect of resonant inverse Compton scattering on the final photon and pair spectra. Both a “warm” hot spot ($T_6 = 1$, $\theta_{\text{spot}} = 0.3$), and a “cool” spot ($T_6 = 0.3$, $\theta_{\text{spot}} = \pi/2$) are considered, as well as the case where ICS is inactive. For the cascade parameters adopted in our simulations, the results for “hot” hot spots ($T_6 = 3$, $\theta_{\text{spot}} = 0.1$) are nearly the same as for warm spots, and so are not shown. This is because the increased cascade activity due to the larger T almost exactly cancels the decreased activity due to the smaller maximum photon-electron intersection angle ψ_{crit} . We find due to resonant ICS, a majority of the electrons and positrons with energies in the range $E_{\text{RICS}} \sim 20\text{--}2000B_{p,12}T_6^{-1}$ MeV [Eq. (53)] radiatively cool to below that range. This has a strong effect on the pair spectra if the average electron/positron energy \bar{E} lies in this range (which occurs, e.g., for $B_{p,12} \lesssim 44.14$ when $P_0 \geq 0.1$ and $\gamma_0 \leq 4$; see Table 2). In general, we find that including RICS tends to make the cascade pair energy distribution narrower. On the other hand, ICS has only a minor effect on the photon spectra; its effect is moderate when $\bar{E} \sim 20\text{--}2000B_{p,12}T_6^{-1}$ MeV and $\mathcal{E}_{\text{tot}} > \epsilon_{\text{tot}}$ (which only occurs when $\mathcal{R}_c = R$ and $B_{p,12} = 10$; see Table 2). Regardless of the cascade parameters, resonant ICS by the secondary particles has very little effect on the multiplicity of photons N_ϵ or

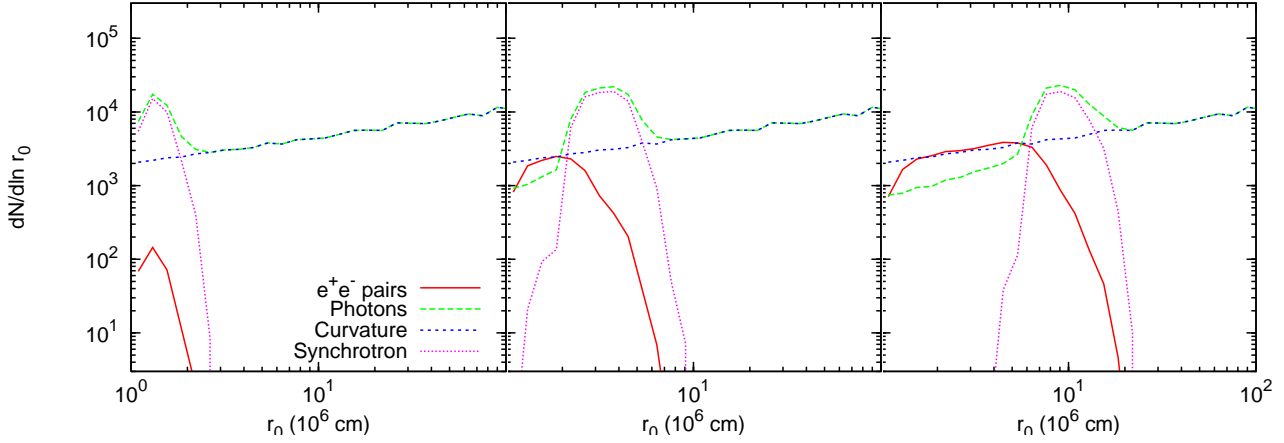


Figure 11. The number of photons and electrons + positrons as a function of the radius where they are created, $r_{0,\text{ph}}$ or r_0 , for $B_{p,12} = 1$ (left panel), 44.14 (middle panel), and 1000 (right panel). The neutron star spin period is assumed to be $P_0 = 1$ and a dipole field geometry is used. The $\perp \rightarrow \parallel$ photon splitting mode is active, and the primary electron has $\gamma_0 = 2 \times 10^7$; the effects of ICS are not included. The curve labeled “ e^+e^- pairs” shows where the secondary electrons and positrons are created, “Photons” shows where the photons that escape the magnetosphere (i.e., that do not split or pair produce) are created, “Curvature” shows where the curvature photons are emitted by the primary electron (which continues in a similar manner beyond the graph out to the light cylinder), and “Synchrotron” shows where the synchrotron photons are emitted by the secondary pairs.

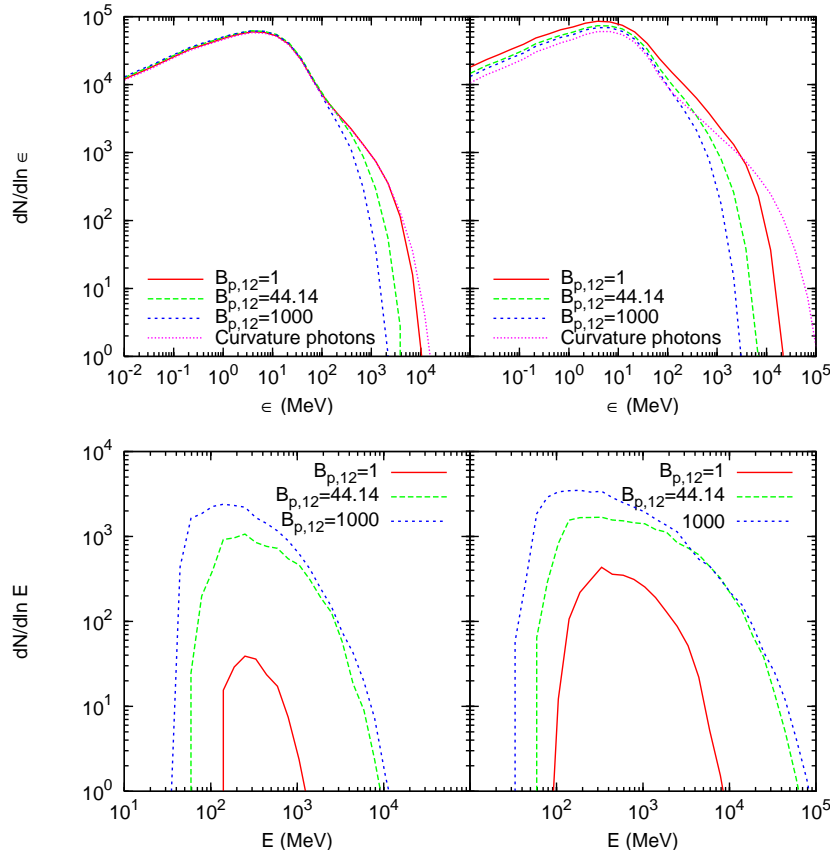


Figure 12. The final photon and pair spectra of electron-initiated cascades. The primary electron has Lorentz factor $\gamma_0 = 2 \times 10^7$ (the left two panels) and 4×10^7 (right two panels), and the surface magnetic field strengths are $B_{p,12} = 1, 44.14,$ and 1000. The neutron star spin period is $P_0 = 1$ and a dipole field geometry is adopted. The secondary photon spectra are shown in the top two panels; the pair spectra are shown in the bottom two panels. The curve labeled “Curvature photons” in each of the top two panels (the dot-dashed line) shows the spectrum of curvature radiation emitted by the primary electron, which is the same for all field strengths.

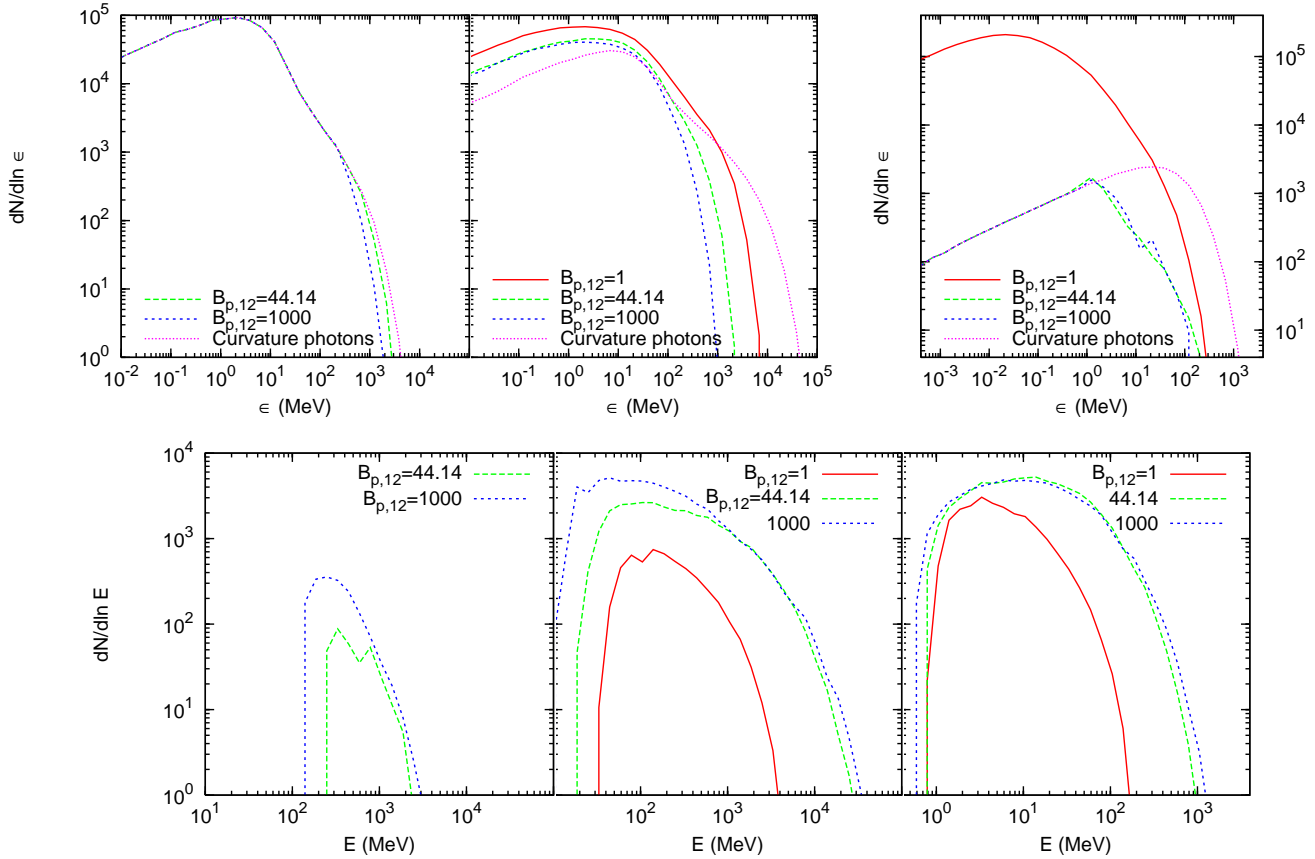


Figure 13. The final photon and pair spectra of electron-initiated cascades for dipole magnetospheres with $P_0 = 10$ (left panels) and 0.1 (middle panels), and non-dipole magnetospheres with $\mathcal{R}_c = R$ (right panels). The surface field strengths are $B_{p,12} = 1, 44.14,$ and 1000 . The Lorentz factor of the primary electron is $\gamma_0 = 2 \times 10^7$ for the dipole magnetospheres (left and middle columns) and $\gamma_0 = 2 \times 10^6$ for the non-dipole magnetosphere (right column; see Section 2). The photon spectra are shown in the top three panels; the pair spectra are shown in the bottom three panels. The curve labeled “Curvature photons” in each of the top three panels (the dot-dashed line) shows the spectrum of curvature radiation emitted by the primary electron, which is the same for all field strengths. Note that the top right panel, corresponding to the photon spectra when $\mathcal{R}_c = R$, has a different vertical (and horizontal) scale than the top left and top middle panels.

pairs N_E created in the cascade, so it does not alter the pulsar death line given by Eq. (58).

Figure 16 shows the effect of photon splitting on the final photon and pair spectra. We consider both the case where photon splitting is allowed only in the $\perp \rightarrow \parallel \parallel$ mode (as discussed in Section 3.2 and in agreement with the selection rule of Adler 1971; Usov 2002), and the case where both \perp and \parallel photons are allowed to split (as is suggested in Baring & Harding 2001). For the cascade parameters adopted in Fig. 16, we find that when photon splitting is “turned off” completely, the spectra are nearly indistinguishable from the case where photon splitting is allowed only in the $\perp \rightarrow \parallel \parallel$ mode. In general, the effect of photon splitting when both polarizations are allowed to split is strongest for large B_p and at high energies (e.g., large γ_0), such that the quantity $x\beta_Q$ is large [see Eq. (28)]. At altitudes where the local field strength is $B \gtrsim 0.5B_Q$ (which occurs, e.g., at $r \lesssim 4R$ for $B_{p,12} = 1000$), most photons continue to split until they reach ϵ_{\min} [Eq. (48) or (54)], and very few pairs are created. However, once the cascade reaches an altitude such that $B < 0.5B_Q$, photon splitting has very

little effect on the cascade. Because a majority of pairs are produced at altitudes above $B \simeq 0.5B_Q$ (see Figs. 11 and 14), the pair spectrum is not strongly affected by photon splitting even when both polarizations are allowed to split and $B_{p,12} = 1000$.

5 DISCUSSIONS

We have presented numerical simulations of pair cascades in the open-field line regions of neutron star magnetospheres, for surface magnetic fields ranging from $B_p = 10^{12}$ G to 10^{15} G, rotation periods $P = 0.1$ – 10 s, and dipole and more complex field geometries. Compared to previous studies (e.g., Daugherty & Harding 1982; Sturmer et al. 1995; Daugherty & Harding 1996; Hibschan & Arons 2001b; Arendt & Eilek 2002), which were restricted to weaker magnetic fields ($B \lesssim$ a few $\times 10^{12}$ G) and dipole geometry, we have incorporated in our simulations additional physical processes that are potentially important (especially in the high field regime) but were either neglected or crudely treated before, including photon splitting with the correct selection

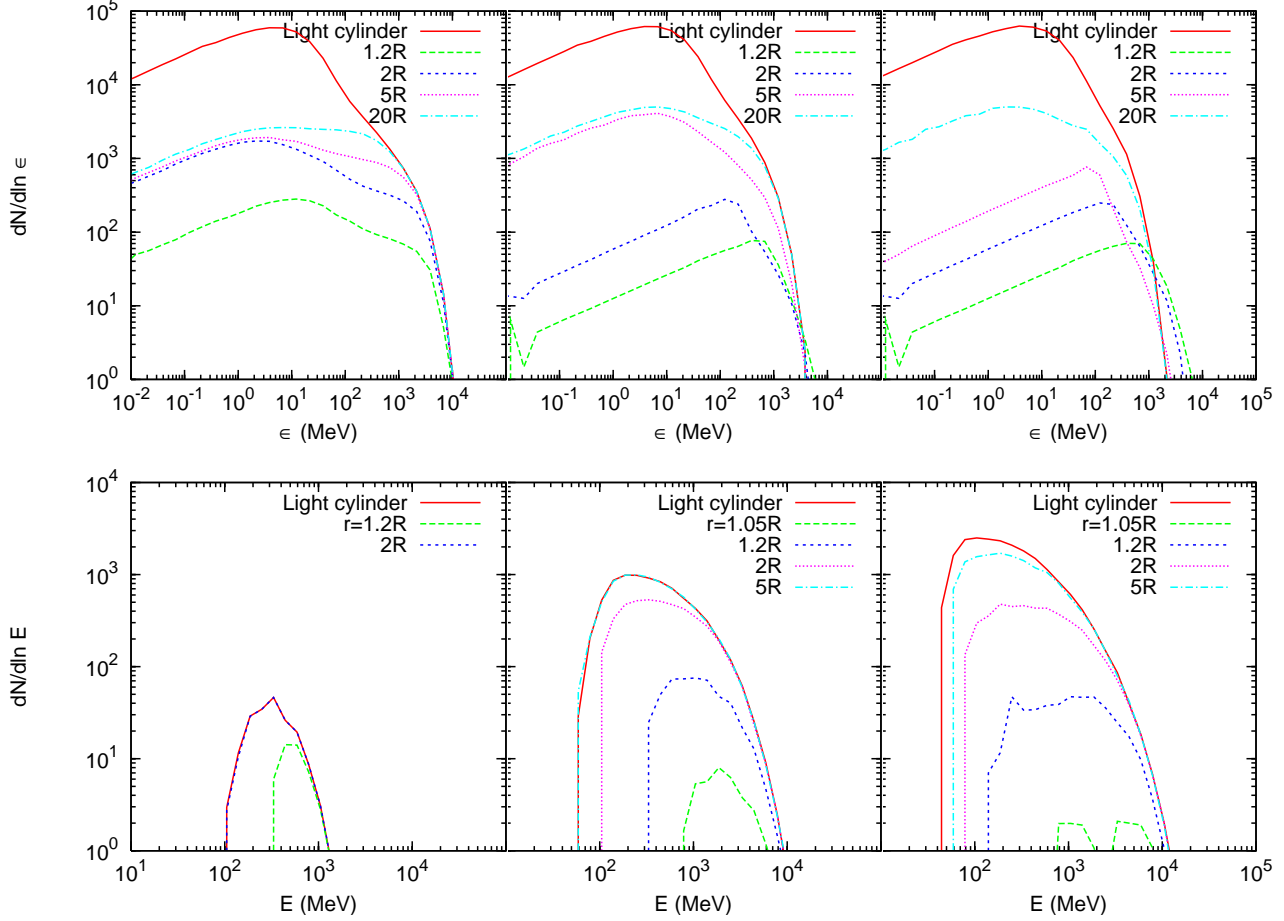


Figure 14. The cumulative photon and pair spectra at magnetosphere radii $r = 1.05R, 1.2R, 2R, 5R, 20R$, and r_{LC} (denoted “Light cylinder”), for $B_{p,12} = 1$ (left two panels), 44.14 (middle panels), and 1000 (right panels). The NS spin period is $P_0 = 1$ and a dipole field geometry is used, and $\gamma_0 = 2 \times 10^7$. The photon spectra are shown in the top three panels; the pair spectra are shown in the bottom three panels. For a given magnetosphere radius r , every cascade particle that is created below r and survives until reaching r is recorded in the spectrum.

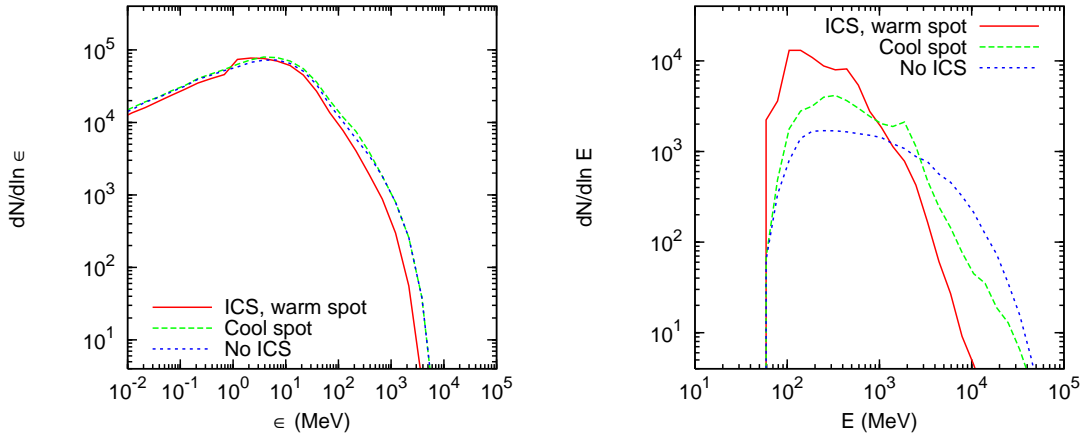


Figure 15. The effect of resonant inverse Compton scattering on the final photon and pair spectra. Two surface hot spot models are considered: a “warm” spot ($T_6 = 1, \theta_{\text{spot}} = 0.3$) and “cool” spot ($T_6 = 0.3, \theta_{\text{spot}} = \pi/2$). The case where ICS is inactive is also shown. The other cascade parameters are: $B_{p,12} = 44.14, P_0 = 1$ (a dipole field geometry is used), and $\gamma_0 = 4 \times 10^7$. The photon spectra are shown in the left panel and the pair spectra are shown in the right panel.

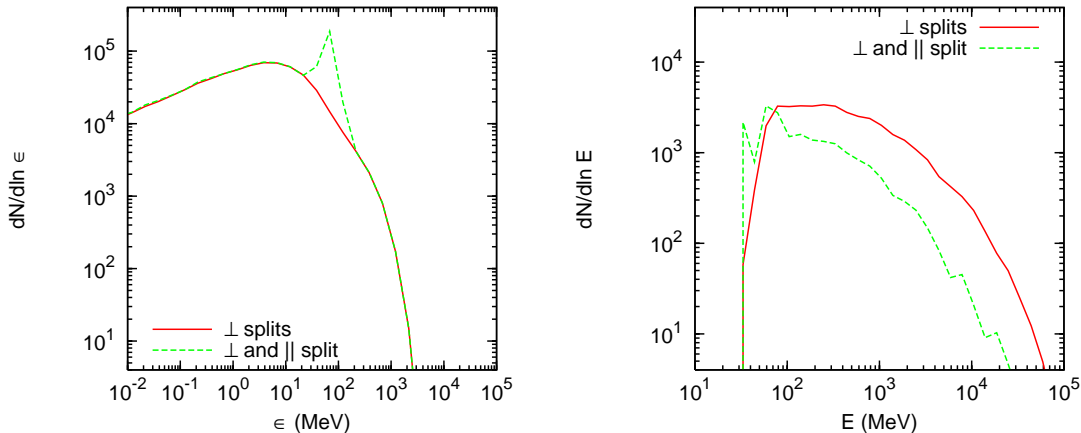


Figure 16. The effect of photon splitting on the final photon and pair spectra. The solid lines show the case where only photons with perpendicular polarizations are allowed to split ($\perp \rightarrow \parallel$), and the dashed lines show the case where photons of both polarizations are allowed to split. The other cascade parameters are: $B_{p,12} = 1000$, $P_0 = 1$ (a dipole field geometry is adopted), and $\gamma_0 = 4 \times 10^7$. The photon spectra are shown in the left panel and the pair spectra are shown in the right panel. For typical cascade parameters, the spectra when photon splitting is “turned off” in the simulation are nearly indistinguishable from the spectra when only $\perp \rightarrow \parallel$ is allowed; we therefore do not present the turned-off case here (but see Fig. 12).

rules for photon polarization modes, one-photon pair production into low Landau levels for the e^\pm , and resonant inverse Compton scattering from polar cap hot spots [with $T = (0.3\text{--}3) \times 10^6$ K]. Both cascades initiated by a single electron (representing the entire cascade process described in Section 1) and by a single photon (representing one branch of the cascade) are simulated, for a variety of initial energies of the primary particle ($\gamma_0 m_e c^2$ and ϵ_0). We have made an effort to present our numerical results systematically, including empirical relations for the pair multiplicity (i.e., the number of electrons and positrons produced per primary particle).

Locally the cascade behaves very differently above and below the critical QED field strength $B_Q \equiv 4.414 \times 10^{13}$ G (e.g., pair production is ~ 10 times more efficient for $B > B_Q$ but synchrotron emission is highly suppressed; see Section 4). Globally, however, the cascade followed from the surface to the light cylinder behaves similarly regardless of surface field strength B_p . For example, we find that the total number of pairs produced in electron-initiated cascades, as well as their energy spectrum, depends on the polar cap voltage $B_p P^{-2}$ but is weakly dependent on B_p alone. Additionally, the total photon spectra for $B > B_Q$ and $B < B_Q$ have similar shapes over the energy range we consider in our simulation (10 keV–1 TeV); this is because curvature radiation, which dominates the photon spectrum over most of this energy range, is independent of magnetic field strength. Photon splitting, a process that is only active for $B \gtrsim B_Q$, could potentially distinguish between neutron stars with high and low surface fields, by lowering the multiplicity of electrons and positrons N_E produced in the cascade to such a degree that the radio emission mechanism can not function (Baring & Harding 2001). However, we find that even if both photons polarized parallel to and perpendicular to the magnetic field are allowed to split, photon splitting lowers N_E by at most 50% for $B_{p,12} = 1000$ and by $< 10\%$ for $B_{p,12} \leq 100$. With the correct selection rule ($\perp \rightarrow \parallel$), the effect of photon splitting is even smaller.

Our results show that a strongly non-dipole magnetic field with radius of curvature $\sim 10^6$ cm near the stellar surface (r less than a few stellar radii) can account for pulsars which lie below the standard death line for dipole fields (see Section 2). Whether or not such a strongly-curved geometry could form is another question altogether. It is doubtful that cascades initiated by resonant inverse Compton scattering in the open field region of the magnetosphere can account for the “missing” pulsars, as the multiplicity of pairs produced in such cascades ($\lesssim 1$ per primary electron) are too low for the current models of the pulsar radio emission. High-multiplicity cascades due to resonant ICS may still occur along twisted lines in the closed field region (where the primary electrons never reach Lorentz factors larger than $\gamma_0 \sim 10^3$), as they do in magnetars (e.g., Thompson et al. 2002; Beloborodov & Thompson 2007; Thompson 2008a,b; Beloborodov 2009).

At any altitude in the magnetosphere, the photon spectrum at low energies ($\lesssim 1$ MeV) has a power-law shape with spectral index $\Gamma = 2/3$ (where $dN/d\epsilon \propto \epsilon^{-\Gamma}$); this is true regardless of whether synchrotron radiation or curvature radiation dominates the spectrum, as both processes have the same low-energy shape. The photon spectrum $dN/d\epsilon \propto \epsilon^{-2/3}$ is harder than the hard X-ray spectra observed in several pulsars, which typically have photon indices $\Gamma \sim 1\text{--}2$ (see, e.g., Kuiper & Hermsen 2009; Bogdanov & Grindlay 2009). One way to reconcile our results with observations is to include an additional radiative process, cyclotron resonant absorption, in the simulation. Such an approach is taken by Harding et al. (2005) (see also Harding et al. 2008), who find that in addition to the synchrotron radiation emitted immediately upon creation, the e^\pm particles emit an additional component of synchrotron radiation at large altitudes that dominates the low-energy spectrum. The efficiency of this high-altitude synchrotron emission is due to the large pitch angles of the e^\pm , which they obtain through resonant absorption of radio photons that are beamed from some intermediate height in the magneto-

sphere. The high-altitude synchrotron emission will have a hard X-ray part with photon index $\Gamma_{10-1000 \text{ keV}}$ generally different from $2/3$, because the hard X-ray band lies near the peak of the emission (rather than in the low-energy tail as is the case for the low-altitude emission). Harding et al. (2005) find that for typical millisecond parameters the photon index is in the observed range, $1 < \Gamma_{10-1000 \text{ keV}} < 2$.

To fully incorporate the effects of cyclotron absorption into our simulation, we would need a model of the radio beam structure and spectrum, since the evolution in the pitch angle of each e^\pm particle depends on the angle at which radio photons of the resonant frequency are incident on the particle and their density. Empirical models of radio beams exist (e.g., Rankin 1993; Arzoumanian, Chernoff, & Cordes 2002; Kijak & Gil 2003); however, inclusion of such a model is beyond the scope of this paper. This means that we can not say anything in detail about the hard X-ray spectra of strongly-magnetized neutron stars, such as whether the high-altitude synchrotron component dominates and what its low-energy cutoff is (but see Harding et al. 2005 for examples of these spectra at several different cascade parameters). Nevertheless, we can use the e^\pm spectra from our simulation to estimate how the $\Gamma_{10-1000 \text{ keV}}$ photon index varies as a function of the cascade parameters. For synchrotron emission from a distribution of e^\pm particles, the hardness of the e^\pm spectrum and the hardness of resulting photon spectrum are correlated [for a $dN/dE \propto E^{-p}$ power-law distribution of e^\pm the photon spectrum has an index given by the familiar expression $\Gamma = (p + 1)/2$]. We find that the e^\pm spectrum is harder, and therefore $\Gamma_{10-1000 \text{ keV}}$ is lower, for larger B_p or γ_0 or shorter P (i.e., anything that increases the energy of the cascade); additionally, for two neutron stars with the same polar cap voltage $B_p P^{-2}$, $\Gamma_{10-1000 \text{ keV}}$ is lower in the neutron star with the stronger surface field. Therefore, in pulsars where the cyclotron absorption – synchrotron emission mechanism dominates the hard X-ray spectrum, the most-strongly magnetized pulsars will have the hardest spectra (lowest photon indices), all other parameters being equal.

Luminous hard X-ray (from 20 keV to several hundreds of keV) emission has also been detected from a number of Anomalous X-ray Pulsars by INTEGRAL and RXTE (e.g., Kuiper et al. 2006). Possible mechanisms for this emission were discussed by Thompson & Beloborodov (2005) and Beloborodov & Thompson (2007). Since the observed hard X-ray luminosity exceeds the spin-down power by several orders of magnitude, it must be fed by an alternative source of energy such as the dissipation of a superstrong magnetic field. We note, however, that the observed photon indices, $\Gamma \sim 0.8 - 1.8$, are similar to (but slightly harder than) those of radio pulsars. Synchrotron radiation by secondary e^+e^- pairs produced in a cascade similar to those studied in this paper could plausibly explain the observations.

In constructing our simulations, we have attempted to rely as little as possible on the precise nature of the acceleration region. However, there are several key assumptions that we have made that are only valid for inner gap accelerators (e.g., that the cascade begins at the neutron star surface). It has become apparent that models where particle acceleration occurs only in the inner gap can not account for the observed high-energy gamma ray emission from young pulsars. For example, the gamma-ray pulse

profiles (e.g., the widely separated double peaks) of the six pulsars detected by EGRET already suggested that models of high-altitude gamma-ray emission were required. More recently, observations of the Crab pulsar by the Major Atmospheric Gamma-ray Imaging Cherenkov Telescope (MAGIC) and around 50 pulsars with “above average” spin-down powers by the Fermi Gamma-ray Space Telescope have revealed that the high-energy tails of the photon spectra fall off exponentially or more slowly than exponential (Aliu et al. 2008; Abdo et al. 2009a,b,c, 2010), while inner gap models predict that the tails fall off faster than exponential (see, e.g., Fig. 12). The outer gap model and the high-altitude version of the slot gap model have been successful in explaining the γ -ray pulsar light curves (e.g., Watters et al. 2009; Venter, Harding, & Guillemot 2009; but see Bai & Spitkovsky 2009).

Although an outer gap or slot gap accelerator model is required to explain gamma-ray observations, our results based on the inner gap model still have general applicability. First, even when the acceleration region is located in the outer magnetosphere a significant fraction of the pair creation must occur in the inner magnetosphere (e.g., Cheng et al. 2000). Indeed, pulsar radio emission is strongly constrained to originate from well inside the light cylinder radius; the only way to generate highly coherent radio emission is to have copious e^\pm plasma produced by vigorous pair cascades (e.g., Melrose 2004; Lyubarsky 2008). Second, both inner gap and outer gap accelerators may exist in a neutron star simultaneously, whether as one extended acceleration region (e.g., Hirovani 2006) or on different field lines. Radio observations suggest that radio emission can come from intermediate field lines, neither along the pole of the star nor at the edge of the open field region (Gangadhara 2004); if this is true, it provides further support for an inner gap origin of the e^\pm plasma, since the plasma generated by an outer gap model is formed on field lines close to the last open field line. In addition, as discussed above, hard X-ray (10-1000 keV) observations of both pulsars and magnetars support a magnetosphere model where the hard X-ray emission is dominated by radiation from the e^+e^- pairs generated by inner gap cascades. Third, it is unlikely that the death lines for the inner gap and outer gap mechanisms overlap completely. There should therefore be regions of the $P-\dot{P}$ diagram where the outer gap mechanism is excluded but the inner gap mechanism still functions; these regions, if they exist, will be located near the inner gap death line, where pulsars have very low spindown powers. Although observations show that the gamma-ray spectra is dominated by slot or outer gap emission for pulsars with moderate to large spindown power, they have not yet ruled out an inner gap origin for pulsars with low spindown power.

ACKNOWLEDGMENTS

ZM has been supported in part by the Lorne Trottier Chair in Astrophysics and Cosmology and an NSERC Discovery Grant awarded to Andrew Cumming. This work forms part of the Ph.D. thesis of ZM at Cornell University. This work has been supported in part by NASA grant NNX07AG81G and NSF grants AST 0707628.

APPENDIX A: RESONANT INVERSE COMPTON SCATTERING

Here we calculate the photon scattering rate for the resonant inverse Compton process, using the simplified model of an electron positioned directly above the magnetic pole (hot spot) and traveling radially outward; see Fig. A1. The resonant cross section for inverse Compton scattering, in the rest frame of the electron before scattering, is

$$\sigma'_{\text{res}} \simeq 2\pi^2 \frac{e^2 \hbar}{m_e c} \delta(\epsilon' - \epsilon_c), \quad (\text{A1})$$

where $\epsilon' = \gamma\epsilon_i(1 - \beta \cos \psi)$, ϵ_i is the photon energy in the ‘‘lab’’ frame, and ψ is the incident angle of the photon with respect to the electron’s trajectory. This cross section is appropriate even for $B > B_Q$, since the resonant condition $\epsilon' = \epsilon_c$ holds regardless of field strength [though at the highest field strengths the prefactor $2\pi^2 e^2 \hbar / m_e c$ in Eq. (A1) serves only as an upper bound to the exact expression; see Gonthier et al. 2000]. The polar hot spot has an angular size of θ_{spot} ; this sets a maximum value for ψ of

$$\cos \psi_{\text{crit}} = \frac{r - R \cos \theta_{\text{spot}}}{\sqrt{r^2 + R^2 - 2rR \cos \theta_{\text{spot}}}}, \quad (\text{A2})$$

where r is altitude of the electron (from the center of the star). The intensity of emission from the hot spot is

$$I_{\epsilon_i}(\psi; r) = \begin{cases} B_{\epsilon_i}(T) = \frac{\epsilon_i^3 / (4\pi^3 \hbar^3 c^2)}{e^{\epsilon_i / kT} - 1}, & \psi < \psi_{\text{crit}}; \\ 0, & \text{otherwise.} \end{cases} \quad (\text{A3})$$

Therefore, the photon scattering rate for the resonant ICS process above a polar hot spot is given by [see, e.g., Eq. (B3) of ML07]

$$\frac{dN_{\text{ph}}}{dt} = \int d\Omega_i \int d\epsilon_i (1 - \beta \cos \psi) \left(\frac{I_{\epsilon_i}}{\epsilon_i} \right) \sigma'_{\text{res}} \quad (\text{A4})$$

$$= \frac{2\pi^2 e^2 \hbar}{m_e c \gamma} \int_{\psi < \psi_{\text{crit}}} d\Omega_i \left(\frac{B_{\epsilon_i}}{\epsilon_i} \right)_{\epsilon_i = \epsilon_c / [\gamma(1 - \beta \cos \psi)]} \quad (\text{A5})$$

$$= \frac{c}{\gamma^2 \beta a_0} \left(\frac{kT}{m_e c^2} \right) \beta_Q \ln \frac{1 - e^{-\epsilon_c / [\gamma(1 - \beta)kT]}}{1 - e^{-\epsilon_c / [\gamma(1 - \beta \cos \psi_{\text{crit}})kT]}}. \quad (\text{A6})$$

APPENDIX B: PAIR PRODUCTION

B1 Kinematics

Consider the pair production of a photon with energy ϵ and angle ψ (the photon – magnetic field intersection angle). In the frame where the photon is traveling perpendicular to the local magnetic field direction (this ‘‘perpendicular’’ frame moves at the velocity $c \cos \psi$ relative to the ‘‘lab’’ frame), the photon has energy $\epsilon' = \epsilon \sin \psi$, and energy conservation demands

$$\epsilon' = E'_j + E'_k = \sqrt{p_z'^2 c^2 + m_e c^2 (1 + 2\beta_Q j)} + \sqrt{p_z'^2 c^2 + m_e c^2 (1 + 2\beta_Q k)}, \quad (\text{B1})$$

where E'_j and E'_k are the energies of the electron and the positron and p_z' is the momentum along the magnetic field

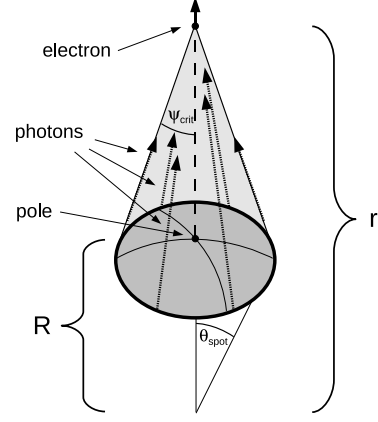


Figure A1. A simplified picture of the ICS effect on the electron. The electron is assumed to be directly above the magnetic pole and travel radially outward.

of either particle ($p'_{z,j} = -p'_{z,k}$). From this we find

$$|p'_z| = m_e c \sqrt{x^2 - 1 - (j+k)\beta_Q + (j-k)^2 \frac{\beta_Q^2}{4x^2}}, \quad (\text{B2})$$

where $x = \epsilon' / (2m_e c^2)$, and

$$E'_j = m_e c^2 \sqrt{x^2 + (j-k)\beta_Q + (j-k)^2 \frac{\beta_Q^2}{4x^2}}, \quad (\text{B3})$$

$$E'_k = m_e c^2 \sqrt{x^2 + (k-j)\beta_Q + (j-k)^2 \frac{\beta_Q^2}{4x^2}}. \quad (\text{B4})$$

In the ‘‘lab’’ frame, the energies of the electron and positron at the moment of pair creation are given by

$$E = \frac{1}{\sin \psi} (E' \pm p'_z c \cos \psi). \quad (\text{B5})$$

In our simulation one particle is randomly assigned the ‘+’ energy and the other the ‘-’ energy, with equal probability of either outcome.

B2 Photon attenuation coefficients and optical depth

In the perpendicular frame, the first three attenuation coefficients for \parallel and the first two non-zero attenuation coefficients for \perp photons are (Daugherty & Harding 1983)

$$R'_{\parallel,00} = \frac{1}{2a_0} \frac{\beta_Q}{x^2 \sqrt{x^2 - 1}} e^{-2x^2 / \beta_Q}, \quad x > 1; \quad (\text{B6})$$

$$R'_{\parallel,01} = 2 \times \frac{1}{2a_0} \frac{2 + \beta_Q - \frac{\beta_Q^2}{4x^2}}{\sqrt{x^2 - 1 - \beta_Q + \frac{\beta_Q^2}{4x^2}}} e^{-2x^2 / \beta_Q}, \quad x > \left(1 + \sqrt{1 + 2\beta_Q}\right) / 2; \quad (\text{B7})$$

$$R'_{\parallel,02} = 2 \times \frac{1}{2a_0} \frac{2x^2}{\beta_Q} \frac{1 + \beta_Q - \frac{\beta_Q^2}{2x^2}}{\sqrt{x^2 - 1 - 2\beta_Q + \frac{\beta_Q^2}{x^2}}} e^{-2x^2 / \beta_Q}, \quad x > \left(1 + \sqrt{1 + 4\beta_Q}\right) / 2; \quad (\text{B8})$$

$$R'_{\perp,01} = 2 \times \frac{1}{2a_0} \frac{\beta_Q}{2x^2} \frac{2x^2 - \beta_Q}{\sqrt{x^2 - 1 - \beta_Q + \frac{\beta_Q^2}{4x^2}}} e^{-2x^2/\beta_Q},$$

$$x > \left(1 + \sqrt{1 + 2\beta_Q}\right)/2; \quad (\text{B9})$$

$$R'_{\perp,02} = 2 \times \frac{1}{2a_0} \frac{x^2 - \beta_Q}{\sqrt{x^2 - 1 - 2\beta_Q + \frac{\beta_Q^2}{x^2}}} e^{-2x^2/\beta_Q},$$

$$x > \left(1 + \sqrt{1 + 4\beta_Q}\right)/2. \quad (\text{B10})$$

Note that $R'_{\perp,00} = 0$. In the above expressions, the attenuation coefficients of Daugherty & Harding (1983) are multiplied by a factor of two for all channels but (00) [i.e., in Eqs. (B7)-(B10)], since we are using the convention $R'_{jk} = R'_{jk}(\text{DH83}) + R'_{kj}(\text{DH83}) = 2R'_{jk}(\text{DH83})$ for $j \neq k$.

We now examine the conditions for pair production by a \parallel -polarized photon; the analysis is similar for a \perp -polarized photon and yields the same result. The optical depth for pair production is

$$\tau = \int_0^{s_{\text{ph}}} ds R(s) = \int_0^{s_{\text{ph}}} ds R'(s) \sin \psi. \quad (\text{B11})$$

We assume $\psi \ll 1$, which is valid since most photons that can pair produce will do so long before the angle ψ approaches unity (only photons with energies $\epsilon \simeq 2m_e c^2$ in the lab frame must wait until $\psi \sim 1$ to pair produce). In this limit, we have $\sin \psi \simeq s/\mathcal{R}_c$, so that x and s are related by

$$x \simeq \frac{s}{\mathcal{R}_c} \frac{\epsilon}{2m_e c^2}. \quad (\text{B12})$$

Let s_{00} to be distance traveled by the photon to reach the first threshold $x = x_{00} \equiv 1$, and s_{01} to be the distance traveled by the photon to reach the second threshold $x = x_{01} \equiv \left(1 + \sqrt{1 + 2\beta_Q}\right)/2$. The optical depth to reach the second threshold for pair production is

$$\tau_{01} = \int_{s_{00}}^{s_{01}} ds R_{\parallel,00}(s) \quad (\text{B13})$$

$$= \frac{\beta_Q}{2a_0} \left(\frac{2m_e c^2}{\epsilon}\right)^2 \mathcal{R}_c \int_{x_{00}}^{x_{01}} \frac{dx}{x\sqrt{x^2-1}} e^{-2x^2/\beta_Q} \quad (\text{B14})$$

$$= 9.87 \times 10^{11} \left(\frac{\mathcal{R}_c}{10^8 \text{ cm}}\right) \left(\frac{100 \text{ MeV}}{\epsilon}\right)^2 T(\beta_Q), \quad (\text{B15})$$

where

$$T(\beta_Q) = \beta_Q \int_{x_{00}}^{x_{01}} \frac{dx}{x\sqrt{x^2-1}} e^{-2x^2/\beta_Q}. \quad (\text{B16})$$

We plot τ_{01} as a function of magnetic field strength in Fig. B1, for $\epsilon = 100$ MeV and $\mathcal{R}_c = 10^8$ cm.

From Fig. B1 we see that pair production occurs in the $(jk) = (00)$ channel ($\tau_{01} \geq 1$) when

$$B \gtrsim B_{\text{crit}} \simeq 3 \times 10^{12} \text{ G}. \quad (\text{B17})$$

Because of the steep dependence of τ on B for $B \sim 3 \times 10^{12}$ G, the value of B_{crit} does not change much for different parameters ϵ and \mathcal{R}_c . For example, $B_{\text{crit}} = 3 \times 10^{12}$ G for $\epsilon = 100$ MeV and $\mathcal{R}_c = 10^8$ cm, and $B_{\text{crit}} = 7 \times 10^{12}$ G for $\epsilon = 10^4$ MeV and $\mathcal{R}_c = 10^6$ cm. Figure B1 also shows that for $B \lesssim B_{\text{crit}}$, the optical depth τ_{01} is much less than unity. The same result is found for the optical depth from the second to the third threshold, and for higher thresholds. The

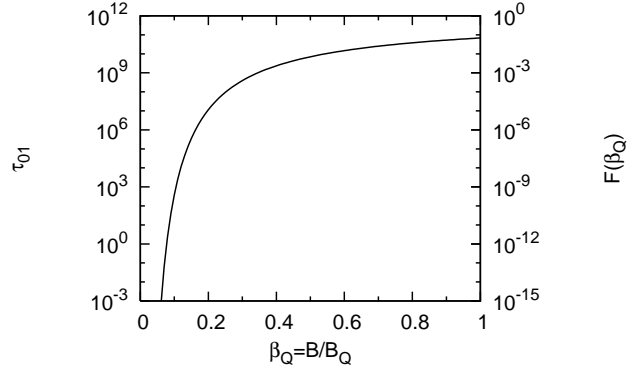


Figure B1. A plot of the function $T(\beta_Q)$ as given by Eq. (B16) (right axis) and the optical depth to reach the second threshold for pair production, τ_{01} (left axis), as a function of β_Q , for $\epsilon = 100$ MeV and $\mathcal{R}_c = 10^8$ cm.

pair production process can therefore be divided into two regimes: for $B \lesssim B_{\text{crit}}$, photons must travel large distances before pair producing, at which point the resulting pairs will be in high Landau levels; for $B \gtrsim B_{\text{crit}}$, photons pair produce almost immediately upon reaching the first threshold, so that the pairs will be in low Landau levels ($n \lesssim 2$).

APPENDIX C: EMPIRICAL RELATIONS FOR THE NUMERICAL RESULTS

In this section we justify several of the empirical relations given in Sections 4.1 and 4.2. In the derivations below we treat the radius of the emission point for the primary photon, $r_6 = r_{0,\text{ph}}/(10^6 \text{ cm})$, as a free parameter. This allows the results to be applicable both to Section 4.1, where we assume that $r_6 = 1$, and to Section 4.2, where $r_6 \geq 1$.

C1 Photon-initiated cascades

At low fields ($B \lesssim B_{\text{crit}} \simeq 3 \times 10^{12}$ G), we can use Eq. (26) for the attenuation coefficient, which implies that pair production occurs when $x\beta_Q \simeq 1/15$ – $1/10$. In the following we will use $x\beta_Q = 1/10$, appropriate for photon energy $\epsilon \sim 10^4$ MeV. To initiate an effective cascade, a photon must pair produce before traveling a distance $s_{\text{ph,max}} = 0.5r_{0,\text{ph}}$ [Eq. (31)]. Therefore the minimum photon energy for cascade is given by

$$\frac{\epsilon_{\text{min}}}{2m_e c^2} \frac{0.5r_{0,\text{ph}}}{\mathcal{R}_c} \simeq \frac{1}{10\beta_Q}, \quad (\text{C1})$$

where β_Q and \mathcal{R}_c should be evaluated at the pair creation point $r \simeq s_{\text{ph,max}} + r_{0,\text{ph}} = 1.5r_{0,\text{ph}}$. Since $\beta_Q = B/B_Q \simeq 0.02B_{p,12}(r/R)^{-3}$ and $\mathcal{R}_c \simeq 10^8 \mathcal{R}_8 \sqrt{r/R}$ cm, where $B_{p,12}$ and \mathcal{R}_8 are the magnetic field strength (in units of 10^{12} G) and curvature radius (in units of 10^8 cm) at the surface, we find

$$\epsilon_{\text{min}} \sim 3000 B_{p,12}^{-1} \mathcal{R}_8 r_6^{5/2} \text{ MeV}. \quad (\text{C2})$$

For a photon injected from the surface ($r_6 = 1$), this reduces to Eq. (48).

In each generation of pair production, a photon of energy ϵ and angle ψ creates an e^\pm pair, each with energy

$\gamma m_e c^2 = 0.5\epsilon$ and traveling in the same direction as the photon. The electron and positron radiate synchrotron photons until they reach an energy of $\gamma_{\parallel} m_e c^2 = m_e c^2 / \sin \psi = \gamma m_e c^2 / x \simeq 0.1 B_{12} \epsilon$, since $x = \gamma \sin \psi \simeq 1/(10\beta_Q)$. The synchrotron photons have a characteristic energy $\epsilon_{\text{SR}} = 1.5\gamma^2 (\sin \psi) \beta_Q m_e c^2 \simeq 0.075\epsilon$. Therefore, in each generation, the energy of the photons and pairs drops by a factor ~ 0.075 while the number of particles increases by $1/0.075$ (see Hibschan & Arons 2001a). When RICS is inactive (e.g., when $T \leq 10^5$ K), such that the only mechanism for energy loss is synchrotron radiation, the final pair spectrum consists of an e^{\pm} pair, each with energy

$$E_{\text{max}} \sim 0.1 B_{p,12} r_6^{-3} \epsilon_0, \quad (\text{C3})$$

created by the primary photon, and a power-law distribution of pairs with index $p \sim 2$ (where $dN/dE \propto E^{-p}$) extending from $\sim 0.075 E_{\text{max}}$ down to $\sim 0.1 B_{12} \epsilon_{\text{min}}$ (see Fig. 6). Hence the total energy of the cascade pairs produced by the primary photon (of energy ϵ_0) is

$$\mathcal{E}_{\text{tot}} \sim 2E_{\text{max}} + 0.1 B_{p,12} r_6^{-3} \epsilon_{\text{min}} n_E \ln \left(\frac{0.075 \epsilon_0}{\epsilon_{\text{min}}} \right). \quad (\text{C4})$$

which reduces to Eq. (52) for $r_6 = 1$.

For the range of high fields considered in this work ($B_{\text{crit}} \lesssim B \leq 1000$), pair production occurs when $x = 1$ (for $x = x_{00}$) or $x \simeq 1-4$ (for $x = x_{01}$; see Section 3.2). For a photon emitted from the point $(r_{0,\text{ph}}, \theta_{0,\text{ph}})$, the maximum intersection angle between the photon and the magnetic field is given by [Eqs. (16), (17), and (21)]

$$\sin \psi_{\text{max}} \simeq \chi [\chi(\theta_{0,\text{ph}})] - \chi(\theta_{0,\text{ph}}) \quad (\text{C5})$$

$$= \arctan \left\{ \frac{1}{2} \tan \left[x + \arctan \left(\frac{\tan \theta_{0,\text{ph}}}{2} \right) \right] \right\}; \quad (\text{C6})$$

for ‘‘small’’ angles $\theta_{0,\text{ph}} \leq 0.6$,

$$\sin \psi_{\text{max}} \lesssim \sin \theta_{0,\text{ph}}. \quad (\text{C7})$$

For $\theta < 0.6$ the local radius of curvature is given by $\mathcal{R}_c \simeq 1.3r / \sin \theta$; therefore, using $x = \epsilon \sin \psi / (2m_e c^2) \sim 2$ we have

$$\epsilon_{\text{min}} \sim 200 \mathcal{R}_8 r_6^{-1/2} \text{ MeV}, \quad (\text{C8})$$

which at $r_6 = 1$ is Eq. (54).

At high fields, each electron-positron pair is created with energies $\gamma m_e c^2 \simeq 0.5\epsilon$ (for \parallel photons) or $\simeq 0.5\epsilon/x_{01}$ and $\simeq 0.5\epsilon(2 - 1/x_{01})$ (for \perp photons). After synchrotron radiation the electron and positron have energies 0.5ϵ or $0.5\epsilon/x_{01}$. Therefore, the final energies of the electron and positron created by the primary photon are given by

$$E_{\text{max}} \simeq \frac{\epsilon_0}{2x_{01}} \text{ or } \frac{\epsilon_0}{2x_{00}} \sim 0.1\epsilon_0 \text{ or } 0.5\epsilon_0. \quad (\text{C9})$$

In order for resonant ICS to modify the cascade spectra, the electron (positron) must have an energy (after synchrotron radiation) larger than the minimum energy at which RICS is effective, i.e., $E_{\text{max}} > 0.3\gamma_{\text{crit}} m_e c^2$ [where $\gamma_{\text{crit}} = \epsilon_c / kT$; see Eq. (53)], which implies

$$\epsilon_0 \gtrsim 70 B_{p,12} T_6^{-1} \text{ MeV}. \quad (\text{C10})$$

C2 Electron-initiated cascades

The spectrum of curvature photons extends from approximately one photon at

$$\epsilon_{\text{max}} \sim 10 \epsilon_{\text{CR}}(\gamma_0) = 3 \times 10^3 \gamma_7^3 \mathcal{R}_8^{-1} \text{ MeV}, \quad (\text{C11})$$

where γ_7 is the primary electron’s initial Lorentz factor γ_0 in units of 10^7 , up to a maximum of $\sim 6 \times 10^4 \mathcal{R}_8^{1/2}$ photons at $\epsilon_{\text{peak}} \sim 6 \mathcal{R}_8^{1/2} \text{ MeV}$. For photon energies below ϵ_{peak} the spectrum is a power law with spectral index $\Gamma = 2/3$ (where $dN/dE \propto E^{-\Gamma}$), characteristic of curvature and synchrotron radiation at low energies (e.g., Erber 1966).

At low fields $B < B_{\text{crit}}$ the pair spectrum extends from

$$E_{\text{max}} \simeq 0.1 B_{p,12} \epsilon_{\text{max}} \sim 300 \gamma_7^3 B_{p,12} \mathcal{R}_8^{-1} \text{ MeV} \quad (\text{C12})$$

down to

$$E_{\text{min}} \simeq 0.1 B_{12} \epsilon_{\text{min}} \sim 300 \mathcal{R}_8 r_6^{-1/2} \text{ MeV}; \quad (\text{C13})$$

at high fields

$$E_{\text{max}} \simeq 0.5 \epsilon_{\text{max}} \sim 6 \times 10^3 \gamma_7^3 \mathcal{R}_8^{-1} \text{ MeV} \quad (\text{C14})$$

and

$$E_{\text{min}} \simeq 0.5 \epsilon_{\text{min}} / x_{01} \sim 20 \mathcal{R}_8 r_6^{-1/2} \text{ MeV}, \quad (\text{C15})$$

(see Section C1).

REFERENCES

- Abdo A. A. et al. (Fermi Collab.), 2009, ApJ, 696, 1084.
 Abdo A. A. et al. (Fermi Collab.), 2009, Science, 325, 848.
 Abdo A. A. et al. (Fermi Collab.), 2009, ApJ, 706, 1331.
 Abdo A. A. et al. (Fermi Collab.), 2010, ApJ, 708, 1254.
 Aliu et al. (MAGIC Collab.), 2008, Science, 322, 1221.
 Adler S. L., 1971, Ann. Phys., 67, 599.
 Arendt P. N., Eilek J. A., 2002, ApJ, 581, 451.
 Arons J., 1996, ApJ, 266, 215.
 Arons J., 1996, A&A, 120, 49.
 Arons J., 1998, in Shibazaki et al., eds, Proc. Intl. Conf. on Neutron Stars and Pulsars, Neutron Stars and Pulsars: Thirty Years after the Discovery. UAP, Tokyo, p. 339.
 Arons J., 2008, in Becker W., ed, Neutron Stars and Pulsars, 40 Years After the Discovery. [arXiv:0708.1050]
 Arons J., Scharlemann E. T., 1979, ApJ, 231, 854.
 Arzoumanian Z., Chernoff D. F., Cordes J. M., 2002, ApJ, 568, 289.
 Bai X.-N., Spitkovsky A., 2009, ApJ, submitted. [arXiv:0910.5741]
 Baring M. G., Harding A. K., 1997, ApJ, 482, 372.
 Baring M. G., Harding A. K., 2001, ApJ, 547, 929.
 Baring M. G., Harding A. K., 2007, Ap&SS, 308, 109.
 Beloborodov A. M., 2008, ApJ, 683, L41.
 Beloborodov A. M., 2009, ApJ, 703, 1044.
 Beloborodov A. M., Thompson C., 2007, ApJ, 657, 967.
 Beskin V. S., 1999, Physics-Uspekhi, 42, 1071.
 Bogdanov S., Grindlay J. E., 2009, ApJ, 703, 1557.
 Camilo F. et al., 2007, ApJ, 669, 561.
 Camilo F. et al., 2008, ApJ, 679, 681.
 Chen K., Ruderman M., 1993, ApJ, 402, 264.
 Cheng K. S., Ho C., Ruderman M., 1986, ApJ, 300, 500.
 Cheng K. S., Ho C., Ruderman M., 1986, ApJ, 300, 522.
 Cheng K. S., Ruderman M., Zhang L., 2000, ApJ, 537, 964.
 Contopoulos I., 2005, A&A, 442, 579.
 Contopoulos I., Kazanas D., Fendt C., 1999, ApJ, 511, 351.
 Contopoulos I., Spitkovsky A., 2006, ApJ, 643, 1139.
 Daugherty J. K., Harding A. K., 1982, ApJ, 252, 337.
 Daugherty J. K., Harding A. K., 1983, ApJ, 273, 761.

- Daugherty J. K., Harding A. K., 1989, *ApJ*, 336, 861.
- Daugherty J. K., Harding A. K., 1996, *ApJ*, 458, 278.
- Dermer C. D. 1990, *ApJ*, 360, 197.
- Dyks J., Rudak B., 2003, *ApJ*, 598, 1201.
- Dyks J., Rudak B., Harding A. K., 2004, *ApJ*, 607, 939.
- Erber T., 1966, *Rev. Mod. Phys.*, 38, 626.
- Gangadhara R. T., 2004, *ApJ*, 609, 335.
- Gangadhara R. T., Gupta Y., 2001, *ApJ*, 555, 31.
- Gonthier P. L., Harding A. K., Baring M. G., Costello R. M., Mercer C. L., 2000, *ApJ*, 540, 907.
- Gruzinov A., 2005, *PRL*, 94, 021101.
- Harding A. K., Baring M. G., Gonthier P. L., 1997, *ApJ*, 476, 246.
- Harding A. K., Muslimov A. G., 2002, *ApJ*, 568, 862.
- Harding A. K., Muslimov A. G., Zhang, B., 2002, *ApJ*, 576, 366.
- Harding A. K., Preece R., 1987, *ApJ*, 319, 939.
- Harding A. K., Stern J. V., Dyks J., Frackowiak M., 2008, *ApJ*, 680, 1378.
- Harding A. K., Tadamaru E., Esposito L. W., 1978, *ApJ*, 225, 226.
- Harding A. K., Usov V. V., Muslimov A. G., 2005, *ApJ*, 622, 531.
- Herold H., Ruder H., Wunner G., 1982, *A&A*, 115, 90.
- Hibschman J. A., Arons. J., 2001, *ApJ*, 554, 624.
- Hibschman J. A., Arons. J., 2001, *ApJ*, 560, 871.
- Hirofani K., 2006, *ApJ*, 652, 1475.
- Kalapotharakos C., Contopoulos I., 2009, *A&A*, 496, 495.
- Kaspi V. M., McLaughlin M. A., 2005, *ApJ*, 618, 41.
- Kijak J., Gil, J., 2003, *A&A*, 397, 969.
- Jackson J. D., 1998, *Classical Electrodynamics*, 3rd edition. Wiley, New York.
- Komissarov S. S., 2006, *MNRAS*, 367, 19.
- Kuiper L., Hermsen W., den Hartog P. R., Collmar W., 2009, *ApJ*, 645, 556.
- Kuiper L., Hermsen W., 2009, *A&A*, 501, 1031.
- Levinson A. et al., 2005, *ApJ*, 631, 456.
- Luo Q., Melrose D., 2008, *MNRAS*, 387, 1291.
- Lyubarsky Y. E., 2002, in Becker W., Lesch H., Trümper J., eds, *Proc. WE-Heraeus Seminar 270, Neutron Stars, Pulsars, and Supernova Remnants*. MPE Rep. 278, p. 230.
- Lyubarsky Y. E., 2008, in Bassa et al., eds, *AIP Conf. Proc. 983, 40 Years of Pulsars: Millisecond Pulsars, Magnetars and More*. AIP, New York, p. 29.
- Lyutikov M., 2007, *MNRAS*, 381, 1190.
- Medin Z., 2008, Ph.D. Thesis, Cornell University, New York.
- Medin Z., Lai D., 2007, *MNRAS*, 382, 1833. [ML07]
- Melikidze G. I., Gil J. A., Pataraya A., 2000, *ApJ*, 544, 1081.
- Melrose D. B., 1995, *J. Astrophys. Astr.*, 16, 137.
- Melrose D. B., 2004, in Camilo F., Gaensler B. M., eds, *Proc. IAU Symp. 218, Young Neutron Stars and Their Environments*. ASP, San Francisco, p.349.
- Muslimov A. G., Harding A. K., 2003, *ApJ*, 588, 430.
- Muslimov A. G., Harding A. K., 2004, *ApJ*, 606, 1143.
- Muslimov A. G., Tsygan A. I., 1992, *MNRAS*, 255, 61.
- Pavan L., Turolla R., Zane S., Nobili L., 2009, *MNRAS*, 395, 753.
- Pons J. A., Link B., Miralles J. A., Geppert U., 2007, *PhRvL*, 98, 1101.
- Rankin J. M., 1993, *ApJ*, 405, 285.
- Rankin J. M., Wright G. A. E., 2003, *A&A Rev.*, 12, 43.
- Romani R. W., 1996, *ApJ*, 470, 469.
- Romani R. W., Yadigaroglu I. A., 1995, *ApJ*, 438, 314.
- Ruderman M. A., Sutherland P. G., 1975, *ApJ*, 196, 51.
- Rybicki G. B., Lightman A. P., 1979, *Radiative Processes in Astrophysics*. Wiley-Interscience, New York.
- Sakai N., Shibata S., 2003, *ApJ*, 484, 427.
- Sokolov A. A., Ternov I. M., 1968, *Synchrotron Radiation*, Pergamon, New York.
- Spitkovsky A., 2006, *ApJ*, 648, 51.
- Sturmer S. J., Dermer C. D., Michel F. C., 1995, *ApJ*, 445, 736.
- Sturrock P. A., 1971, *ApJ*, 164, 529.
- Takata J., Shibata S., Hirofani K., Chang H. K., 2006, *MNRAS*, 366, 1310.
- Thompson C., 2008, *ApJ*, 688, 1258.
- Thompson C., 2008, *ApJ*, 688, 499.
- Thompson C., Beloborodov A. M., 2005, *ApJ*, 634, 565.
- Thompson C., Lyutikov M., Kulkarni S. R., 2002, *ApJ*, 574, 332.
- Thompson D. J. et al., 1999, *ApJ*, 516, 297.
- Thompson D. J., 2004, in Cheng K. S., Romero G. E., eds, *Cosmic Gamma-Ray Sources*. Kluwer, Dordrecht, p. 149.
- Thompson D. J., 2008, in *40 Years of Pulsars: Millisecond Pulsars, Magnetars, and More*. AIP Conf. Proc. No. 983. AIP, New York, p. 56.
- Timokhin A. N., 2006, *MNRAS*, 368, 1055
- Usov V. V., 2002, *ApJ*, 572, L87.
- von Hoensbroech A., Lesch H., Kunz T., 1998, *A&A*, 336, 209.
- Vransevsev N., Manchester R. N., Melrose D. B., 2007, in Becker W., Huang H. H., eds, *Proc. WE-Heraeus Seminar 363, Neutron Stars and Pulsars*. MPE Rep. 291, p. 88.
- Venter C., Harding A. K., Guillemot L., 2009, *ApJ*, 707, 800.
- Watters K. P., Romani R. W., Weltevredre P., Johnston, S., 2009, *ApJ*, 695, 1289.
- Woods P. M., Thompson, C., 2006, in Lewin W., van der Klis M., eds, *Compact Stellar X-ray Sources*. Cambridge Univ. Press, p. 547.
- Zhang, B., Harding, A. K., 2000, *ApJ*, 532, 1150.